

2009

Dynamics of plume formation with through thin film ablation

Kristin M. Bailey
University of Dayton

Follow this and additional works at: https://ecommons.udayton.edu/graduate_theses

Recommended Citation

Bailey, Kristin M., "Dynamics of plume formation with through thin film ablation" (2009). *Graduate Theses and Dissertations*. 1353.

https://ecommons.udayton.edu/graduate_theses/1353

This Thesis is brought to you for free and open access by the Theses and Dissertations at eCommons. It has been accepted for inclusion in Graduate Theses and Dissertations by an authorized administrator of eCommons. For more information, please contact mschlangen1@udayton.edu, ecommons@udayton.edu.

**DYNAMICS OF PLUME FORMATION WITH
THROUGH THIN FILM ABLATION**

Thesis

Submitted to

The School of Engineering of the

University of Dayton

in Partial Fulfillment of the Requirements for

The Degree

Master of Science in Electrical Engineering

by

Kristin M. Bailey

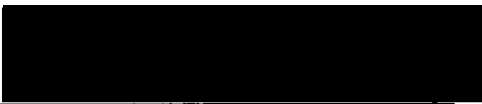
UNIVERSITY OF DAYTON

Dayton, Ohio

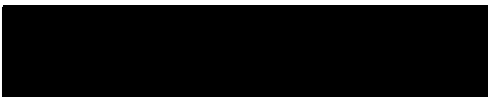
May, 2009

DYNAMICS OF PLUME FORMATION WITH THROUGH THIN FILM ABLATION

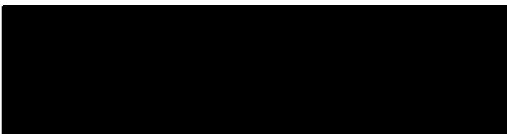
APPROVED BY:




Elena Guliants, Ph.D.
Advisory Committee Chairperson
Professor, Electrical and Computer
Engineering Department




Paul T. Murray, Ph.D.
Committee Member
Professor, Graduate Materials
Engineering Department



Russell C. Hardie, Ph.D.
Committee Member
Professor, Electrical and Computer
Engineering Department



Malcolm W. Daniels, Ph.D.
Associate Dean
School of Engineering



Joseph E. Saliba, Ph.D., P.E.
Dean, School of Engineering

© Copyright by
Kristin M. Bailey
All rights reserved
2009

ABSTRACT

DYNAMICS OF PLUME FORMATION WITH THROUGH THIN FILM ABLATION

Name: Bailey, Kristin M.
University of Dayton

Advisor: Dr. Elena Guliants

Through Thin Film Ablation (TTFA) is a novel variation on pulsed laser deposition to deposit nanoparticles by irradiating a thin film from the backside. The purpose of this study is to characterize TTFA with a picosecond ablation laser, with particular regards to the influence of the energy density and background pressure on the plume formation and dynamics. Measurements were taken on the time of flight of the plume and the charge seen within the plume, and gated optical images were collected in a variety of conditions. This allowed for the formulation of an understanding of the TTFA process and the differences found under various conditions.

ACKNOWLEDGEMENTS

This research was supported by the Air Force Office of Scientific Research under contract number FA9550-07-C-0020, with additional support and equipment provided by Mound Laser & Photonics Center, Inc.

I would like to thank my committee for their expertise and patience in bringing this work to a conclusion, and particularly Dr. Paul T. Murray for providing excellent technical advising and support. I would also like to thank my friends and family for their love and encouragement, with an especially deep debt of gratitude to Richard A. Bailey and Robert Masterson.

TABLE OF CONTENTS

ABSTRACT	iii
ACKNOWLEDGEMENTS	iv
TABLE OF CONTENTS	v
LIST OF FIGURES	vii
CHAPTER 1 - INTRODUCTION	1
CHAPTER 2 - BACKGROUND	6
2.1 - Laser-Material Interaction	6
2.2 - Plume Formation, Development and Measurement	7
2.3 - Ultra Fast Ablation	7
2.4 - Nanosecond TTFA	8
CHAPTER 3 - PURPOSE OF THIS WORK	15
CHAPTER 4 - EXPERIMENTAL	16
4.1 - Equipment	16
4.2 - Measurement Techniques	19
4.3 - Preliminary Experimentation	22
CHAPTER 5 - RESULTS	29
5.1 - PMT Measurements and Speed Calculations	29
5.1.1 - PMT Measurements with Laser Focus at the Target	33
5.1.2 - PMT Measurements with the Laser Focus below the Target	42
5.2 - Charge Plate Measurements	47
5.2.1 - Charge Plate Measurements with the Laser Focus at the Target	49
5.2.2 - Charge Plate Measurements with the Laser Focus below the Target	52
5.3 - Optical Images of Ablation	54

5.3.1 - Optical Images with the Laser Focus at the Target	56
5.3.2 - Optical Images with the Laser Focus below Target	61
CHAPTER 6 - DISCUSSION	66
6.1 - Affect of Film Thickness and Background Pressure	66
6.1.1 - Affect of Film Thickness	66
6.1.2 - Affect of Background Pressure	66
6.2 - Effect of Laser Focus Location	72
6.2.1- Laser Focus below the Target	75
6.2.2 - Laser Focus at the Target	82
CHAPTER 7 - CONCLUSION	91
7.1 - Ablation with the Focal Point below the Target	91
7.2 - Ablation with the Focal Point at the Target	91
CHAPTER 8 - RECOMMENDATIONS FOR FUTURE WORK	93
REFERENCES	94

LIST OF FIGURES

Figure 1.1 - Schematic drawing of a traditional PLD setup	4
Figure 1.2 - Schematic drawing of the setup for TTFA	5
Figure 2.1 - Schematic of the TTFA process	10
Figure 2.2 - TEM of nanoparticles created by picosecond TTFA, with a chart of their measured diameters	11
Figure 2.3 - Setup of the PMT measurements for nanosecond TTFA	12
Figure 2.4 - PMT measurements for nanosecond TTFA	13
Figure 2.5 - Spectral information of the plume for ablation in vacuum.	14
Figure 4.1 - Illustration and picture of the experimental setup and equipment	18
Figure 4.2 - Schematic illustration of the setup with the plume being observed by a PMT	20
Figure 4.3 - Schematic of the metal plate setup	21
Figure 4.4 - Schematic drawings of each setup	24
Figure 4.5 - SEM micrograph of particles formed with the laser focus at the film	25
Figure 4.6 - White light interferometer data of an ablated spot.	26
Figure 4.7 - SEM micrograph of particles formed with laser focal point below target film	27
Figure 4.8 - White light interferometer data showing the removed film	28
Figure 5.1 - A schematic illustration of the setup with the plume being observed by a PMT	30
Figure 5.2 - Plot of the intensity of the plume for both a 10 nm iron film and 25 nm iron film	31
Figure 5.3 - Plot of the PMT signal over a long time interval	32
Figure 5.4 - PMT signal from an iron film ablated in vacuum with laser focus set at film	35
Figure 5.5 - Ablation in 1.33 Pa of argon	36
Figure 5.6 - Ablation in 13.33 Pa of argon	37
Figure 5.7 - Ablation in 66.66 Pa of argon	38

Figure 5.8 - Ablation in vacuum at a distance of 20 mm	39
Figure 5.9 - Ablation with a distance of 20 mm in 13.33 Pa of argon	40
Figure 5.10 - Ablation in 66.66 Pa of argon at a distance of 20 mm	41
Figure 5.11 - Schematic illustration of the setup for the PMT collections with the laser focus below the film	43
Figure 5.12 - Ablation in vacuum with the laser focus below the film	44
Figure 5.13 - Ablation in vacuum with the laser focus below the film, shortly after laser pulse	44
Figure 5.14 - Ablation in 13.33 Pa of argon	45
Figure 5.15 - Ablation viewed at a distance of 20mm in vacuum	46
Figure 5.16 - Ablation in 13.33 Pa of argon	46
Figure 5.17 - Schematic of the metal plate setup	48
Figure 5.18 - Plot of the charge of the metal plate with the laser focus at the film	50
Figure 5.19 - Plot of the change in charge of the metal plate at 20mm distance	51
Figure 5.20 - Signal from the metal plate at a distance of 5mm	53
Figure 5.21 - Signal from the metal plate at a distance of 20 mm	53
Figure 5.22 - A sample image, showing the target and substrate	55
Figure 5.23 - Images collected at various delays	57
Figure 5.24 - Images collected at various delays at a pressure of 1.33 Pa	58
Figure 5.25 - Images collected at various delays of pressure of 13.33 Pa	59
Figure 5.26 - Images collected at various delays at a pressure of 66.66 Pa	60
Figure 5.27 - Images collected with the laser focus below the film in vacuum	62
Figure 5.28 - Images collected at various delays at a pressure of 1.33 Pa	63
Figure 5.29 - Images collected at various delays at a pressure of 13.33 Pa	64
Figure 5.30 - Images collected at various delays at a pressure of 66.66 Pa	65
Figure 6.1 - Signals captured by the PMT of the plume in various levels of background gas	69
Figure 6.2 - PMT signals from ablations with the laser focus below the film at various pressures	70
Figure 6.3 - Gated camera image with a delay of 1 μ s	71

Figure 6.4 - Peaks seen by PMT when the laser focus is at the target	73
Figure 6.5 - No peaks seen by PMT when laser focus is below the target	73
Figure 6.6 - Slight peak seen in longer temporal regions when the laser focus is below the target	74
Figure 6.7 - No peaks seen in longer time scales when the laser focus is at the target	74
Figure 6.8 - Velocity and Maxwell-Boltzmann distribution of PMT signal	78
Figure 6.9 - An intensity plot of the emission of the plume at a 1 μ s gate delay	79
Figure 6.10 - SEM micrograph of particles formed with the laser focal point below the target film.	80
Figure 6.11 - White light interferometer data showing the film removed from the substrate	81
Figure 6.12 - Plot of the charge of the metal plate with the laser focus at the film	87
Figure 6.13 - Velocity plot and Maxwell-Boltzmann distribution of the PMT signal	88
Figure 6.14 - Image of the first plasma, dispersing while the second plume forms	89
Figure 6.15 - White light interferometer data of an ablated spot with the laser focal point at the target	90

CHAPTER 1

INTRODUCTION

Since its invention, the laser has come to play a central role in many aspects of technology, including communication systems, holography, measurements and imaging, medicine, consumer products and others. One specific field improved by the application of laser technology is material processing and modification. While this is still a large field, including laser welding, cutting, machining, drilling, cladding, annealing and marking, the ability of lasers to miniaturize features gives laser technology an advantage over traditional methods [1]. The use and application of high power, ultra-short laser pulses opens even more possibilities within the technology [2, 3, 4]. One interesting application of the miniaturization leads to nanofabrication, which is the creation of structures measured on the nanoscale, such as thin film deposition and nanoparticle generation.

Several methods can be used for deposition of thin films. For example, several thermal processes are available, where the material to be deposited as a film is heated, either by passing a current through the material or some other method. The vapor is deposited on a substrate to form the film. While simple, this method has several drawbacks, such as the need for ultra high vacuum to maintain film purity, and the risk of contamination by vapor from the support structure holding the material [5]. Another deposition method is sputtering, where the target is the cathode and the substrate for the film is an anode, with a potential difference as much as several hundred volts between them. This begins a plasma discharge, causing the positive ions to strike the target and sputter off material to arrive at the substrate as neutral atoms. However, a background gas must be used to control the energy of the atoms, and to initiate the plasma [6]. Other chemically based methods are also used. For example, in chemical vapor deposition (CVD), several component materials are transported to a heated substrate in the vapor phase and utilize the thermal energy for the chemical reactions necessary to form a film of desired composition.

However, the composition of films is limited to the chemical reactions available, and the temperatures needed are often on the order of several hundred degrees centigrade [6].

In contrast, pulsed laser deposition (PLD) can utilize the precision and control available from using a laser system in the creation of the films and nanoparticles. As can be seen in Figure 1.1, the set up for PLD is simple, with a pulsed laser beam focused to strike a solid target at an angle. With a high energy density at the target surface, the material melts and vaporizes, absorbing energy to form a plasma consisting of atoms, ions and molecules, which travel perpendicular to the target surface to settle on the substrate with initial speeds of 10^4 meters per second [7]. This provides numerous advantages, such as only heating the target material, and not a support structure. The films created have the same stoichiometric composition as the target [8]. Nanoparticles are also easily formed by PLD, as larger atom clusters are commonly formed in the ablation process, with some ability to control the particle size [9].

However, there are several main disadvantages to PLD, including cumulative heating in the target from repetitive laser pulses, absorption of the laser energy by the plume, agglomeration from adiabatic expansion of the plasma out of the creator created by the laser pulse, lack of control of the amount of material removed with each laser pulse, and an inability to control particle size.

One specific application of PLD is growing carbon nanotubes (CNTs) [10, 11]. CNTs have many valuable applications, such as conductive and high-strength composites, miniaturizing semiconductor devices and interconnects and memory components and transistors [6, 12]. However, CNTs require not only a carbon source, but a catalyst nanoparticle for growth. The catalyst composition and size can have a profound effect on the created nanotubes, causing variations in number of walls, length, and diameters [13, 14, 15]. While it has been shown that CNTs can be formed from a single laser pulse [16], a better PLD system would reduce the need for post-processing and purification of the nanotubes, as well as improving the efficiency of the CNT growth process by reducing contaminants and increasing growth rates.

A variation of PLD, Through Thin Film Ablation (TTFA) improves upon several disadvantages of traditional PLD. Invented by P.T. Murray and L.R. Dosser, the work presented

in this thesis is the first detailed study of the properties and characteristics of TTFA performed with a picosecond laser. It is set up such that a thin film, on the order of tens of nanometers in thickness and supported by a transparent substrate, is ablated from the backside, with the laser energy being deposited through the transparent support. A schematic representation is shown in Figure 1.2. The plume that is generated remains highly directional, but contains a known amount of material, as the film thickness becomes the crater depth. There is also no agglomeration of the material, as the film is too thin to create adiabatic expansion out of the hole. There is also minimal creation of larger ($>1\mu\text{m}$) particles as the film is too thin to create a large melt layer in the target surface [17].

The purpose of this work is to characterize the constituents created by TTFA using a picosecond laser, and to provide an understanding of the processes involved.

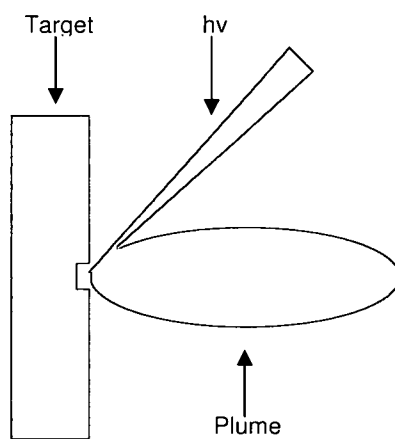


Figure 1.1. Schematic drawing of a traditional PLD setup.

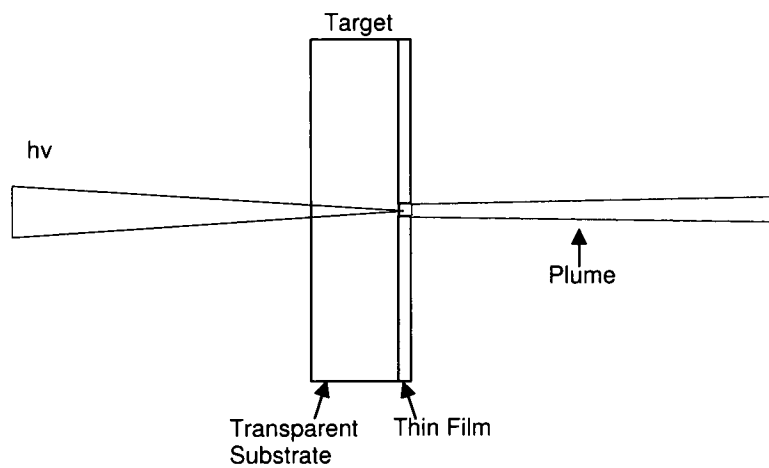


Figure 1.2. Schematic drawing of the setup for TTFA.

CHAPTER 2

BACKGROUND

Pulsed laser deposition (PLD) is a well characterized process (see [18] or [19]), with a lot of study into the laser-material interaction, the plume formation and development, and differences between nanosecond and ultra-fast ablation. In addition, preliminary characterization of Through Thin Film Ablation (TTFA) constituents has been performed on materials created with a nanosecond laser.

2.1 – Laser-Material Interaction

With traditional PLD, a bulk target is irradiated with a laser from an angle, projecting a plume perpendicular to the front of the bulk material. This method creates a melted layer of material within the target, which forms large (micron sized) particles by a process referred to as “splashing” [20]. Some methods have been developed to reduce this effect [21], but there is not a solution. The highly forward nature of the plume deposits material in a non-uniform distribution, requiring moving the beam over the target in a raster pattern or moving the substrate during the ablation to provide an even layer of material [22]. The nature of the crater formed during the ablation also varied the directionality of the plume, as the ejected material moves perpendicular to the ablated surface, and a rougher target causes less predictability in the beam direction. Increasing the laser energy increases the crater depth and width [23, 24]. The laser wavelength will affect the size of the created nanoparticles as the material will have different absorption coefficients at different wavelengths [25].

The damage threshold describes the amount of energy necessary to damage the surface of the target, and is controlled by surface melting [26], but the physical mechanism that causes the breakdown is avalanche ionization, which is a function of the pulse length of the laser [27]. This damage region has been studied with interferometry, optical transmission and acoustic

measurements [28, 29]. The amount of laser energy used to remove material plays an important part in the material removal process, as exemplified when looking at film removal [30, 31].

2.2 – Plume Formation, Development and Measurement

A plume is formed during the laser-material interaction which consists of atoms, ions and particles removed from the surface to create a deposit on the substrate. The evolution of this plume can be measured with gated optical images or emission spectroscopy [32, 33, 34], indicating that the plume follows adiabatic expansion of a gas cloud. Time of Flight data (TOF) measures the time for plasma constituents to form, providing information on the velocity of the emitting particles [35]. Ions contained in the plume material can be measured with a biased Faraday cup, giving a charge measurement over time to identify created species [36]. Rydberg atoms may be formed in the plasma from electron-ion recombination or neutral atoms excited from collisions or photons. They are highly excited, metastable, neutral atoms, detectable by emission spectrometry or quadrupole mass spectroscopy when the atoms are ionized by a deflection charge plate [37].

In describing the kinetic properties of the removed material, a Maxwell-Boltzmann distribution can be fitted to velocity data on the plume if the plume is in equilibrium. The temperature of the plume and the most probable velocity of the material can be found from this fitting [38].

2.3 – Ultra-fast Ablation

Ultra-fast laser ablation provides a separation in time from the laser-material interaction and the removal of the material from the target [39]. More nanoparticles are evident in ablation with ultra-short lasers, often with several plume components with varying velocities [40, 41, 42]. The plume appears more narrow and elongated as compared to ablation with a nanosecond laser source [43].

As compared to ablation with nanosecond pulses, there is a negligible amount of thermal heating in ultra-short pulses. This allows for a very rapid vaporization and plasma formation without a liquid phase [44], which also allows for complete energy distribution in the target without laser-plasma interaction, increasing the volume of material removed by each pulse [45].

Changing the power of the ablation laser creates different regions of ablation, where the ablation region and depth is determined by either the optical or the heat penetration depth [46]. This can result in ultrafast (<1 ps) solid to liquid transformations when ablated with high energy densities [47], causing a plasma to form on the target surface [48].

2.4 – Nanosecond TTFA

TTFA was developed as an alternative to pulsed laser deposition (PLD). In TTFA, a laser strikes the back side of a thin film, deposited onto a transparent substrate, breaking the film apart into a plume composed of atoms that recombine into nanoparticles as they travel to a substrate. This prevents agglomeration of the particles, as there is not a crater for the material to expand out from, which is a disadvantage to PLD. A schematic of this process is shown in Figure 2.1. TTFA also provides a known amount of material in the reaction, as the film is a very specific depth, rather than a deep crater with little depth control from a bulk target, and the laser footprint is known. As there is a very thin layer of material to absorb the laser energy, the particles created are small (<10s of nm in diameter), well dispersed, and not agglomerated [17]. A TEM micrograph of particles created by picosecond TTFA in vacuum, with a chart of the measured particle diameters, is shown in Figure 2.2 [49]. The particles have a most probable diameter of 5 nm.

Some measurements on the TTFA plume constituents have been preformed, using a nanosecond laser as the ablation source. The laser was an excimer laser ($\lambda = 248$ nm), with a pulse duration of 25 ns. The energy density for each ablation was 0.5 J/cm^2 . A 20 nm iron film was used as the target, and a photomultiplier tube (PMT) and a calibrated spectrometer were set up to examine a narrow region of the plume 25 mm away from the target. A schematic of this setup can be seen in Figure 2.3 [50].

Two pressures were used to measure the optical emission as seen by the PMT. The first was done in vacuum, and the second preformed in 66.66 Pa of static argon as a background gas. As can be seen in Figure 2.4 (a), the ablation in vacuum showed a peak near time 0 from the scattering of the laser light, with a secondary peak approximately 50 μs after the laser pulse. This corresponds to a velocity of 500 m/s. In contrast, Figure 2.4 (b) shows the emission from the

plume ablated in 66.66 Pa. Similarly, there is an initial peak from the laser light scattering, and a peak at 50 μ s. However, there is another peak at 10 μ s, which corresponds to a speed of 2.5 km/s [50].

Measuring the spectral response for the ablation in vacuum gave a varying function of wavelength, shown in Figure 2.5. No atomic or molecular emission lines are seen, but the curve can be fit to the equation for black body radiation to determine the temperature of the plume. This fitting is shown by the solid line, for a temperature of 2232 K. Similar results were found for a 50 μ s delay after the laser pulse for the ablation in 66.66 Pa of argon, but at shorter delays (\sim 3 μ s) atomic iron peaks were seen [50].

The temperature found for the plume, 2232 K, is interesting in that this is higher than the melting temperature of iron, 1811 K, but lower than the boiling point, 3134 K. This indicates that the fast peak in the PMT signal contains atomic and molecular iron, while the slower peak emits black body radiation from molten iron nanoparticles [50].

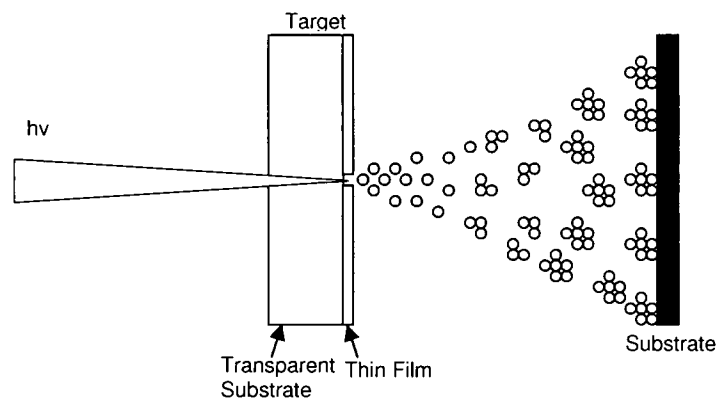


Figure 2.1. Schematic of the TTFA process.

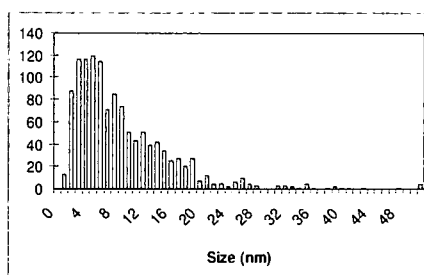
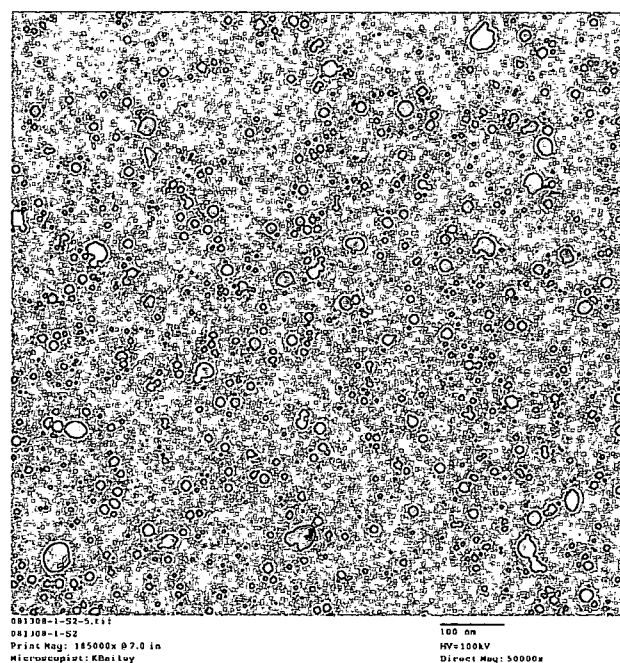


Figure 2.2. TEM of nanoparticles created by picosecond TTFA, with a chart of their measured diameters.

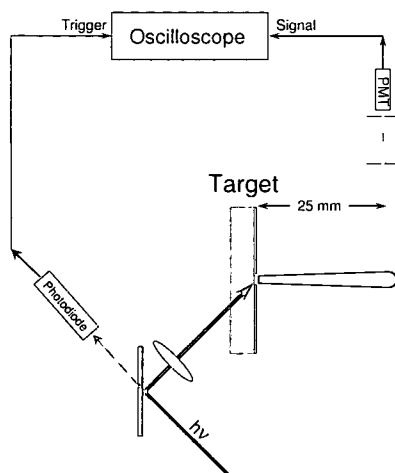


Figure 2.3. Setup of the PMT measurements for nanosecond TTFA.

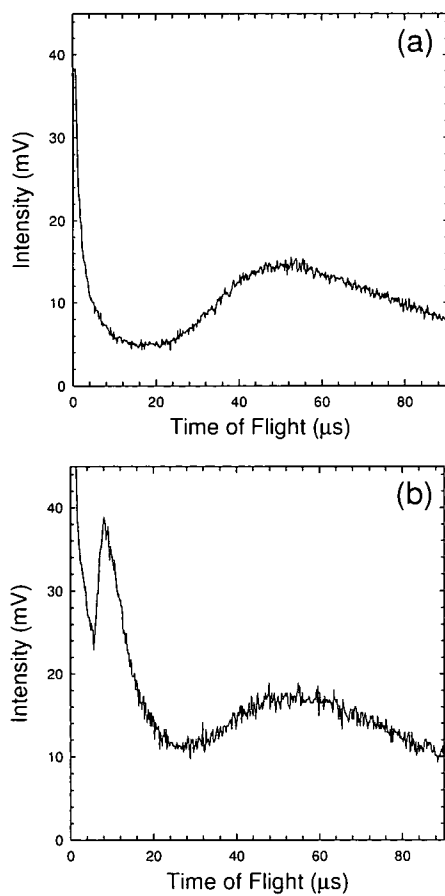


Figure 2.4. PMT measurements for nanosecond TTFA in (a) vacuum and (b) in 66.66 Pa of argon.

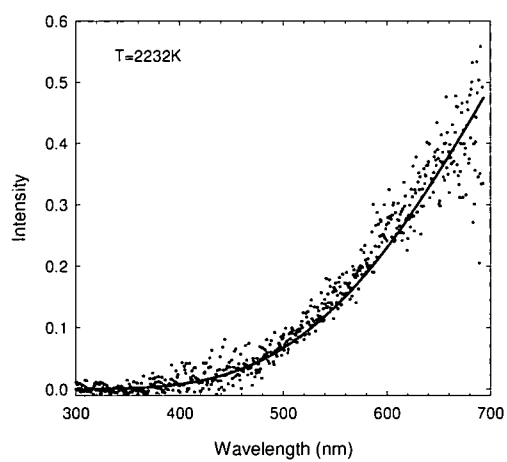


Figure 2.5. Spectral information of the plume for ablation in vacuum. The solid line is a fit to the black body equation, for a temperature of 2232 K.

CHAPTER 3

PURPOSE OF THIS WORK

The purpose of this work is to characterize the plume constituents created by Through Thin Film Ablation (TTFA) by using a picosecond laser and provide an understanding for the processes in effect. The fundamental observations that lead to this work were the differences in the ablation mechanism created by changing the location of the laser focal point relative to the target. During this course of study, the following questions will be examined and answered:

1. What affect does the location of the focal point have on the ablation process?
2. For each location of focus, can an understanding of the process be formulated?
3. Does the background pressure during the ablation have an effect on the plume dynamics?

To answer these questions, the following measurements will be made:

1. The apparent speed of the ablation constituents as measured by a PMT,
2. The charge of the constituents,
3. Optical images of the constituents at various delays to analyze the temporal development of the plume.

CHAPTER 4

EXPERIMENTAL

4.1 – Equipment

For the experimentation presented here, a solid state Nd:YVO₄ laser was used as the energy source. The laser is a Lumera Super Rapid, with 8W maximum power at a wavelength of 1064 nm. The output beam has a Gaussian energy distribution through the beam axes and a pulse duration of 12-14 ps. The laser was operated at 1.176 kHz with an average power of 151 mW. The laser was focused onto the target with a 331 mm focal length lens attached to a scan head. The scan head consisted of two galvo mirrors to direct the beam in both the x and y direction, allowing precise positioning of the beam on the target surface. An illustration and a picture of the setup are shown in Figure 4.1, with the beam path highlighted.

The height of the scan head could be adjusted such that the location of the focal point of the laser could be changed relative to the target. This predominately affected the spot size of the laser on the target, which in turn affected the calculated energy density of the laser. All experiments were performed inside a vacuum chamber, allowing for variation of the background pressure and gas type. The chamber had eight side ports allowing for several view ports and other inputs for measuring and monitoring equipment. The target and the substrate were held 59.6 mm apart by an assembly inside the chamber.

The targets were composed of a thin film of iron on a one inch round support of UV-grade quartz. The films were sputtered onto the support by a calibrated method from a pure iron target and the calibration was checked with a stylus profilometer. After ablation, the area of the removed material was measured with a calibrated reticle inserted into the eyepiece of the optical microscope. The depth of the removed material was measured on a white light interferometer, a

Wyko NT1100 from Veeco Instruments, and verified with a Veeco Dektak 6M surface profilometer.

The material in the plume was captured on a substrate that consisted of both carbon-coated copper grids suitable for transmission electron microscopy (TEM) and a small section of a silicon wafer for scanning electron microscopy (SEM). The instruments used for the analysis were a Hitachi H-7600 TEM, operating at a filament current of 100kV, and a Hitachi S-4800 High Resolution SEM. Micrographs and other images were analyzed using ImageJ, a Java-based image analysis and processing tool developed by Wayne Rasband [51].

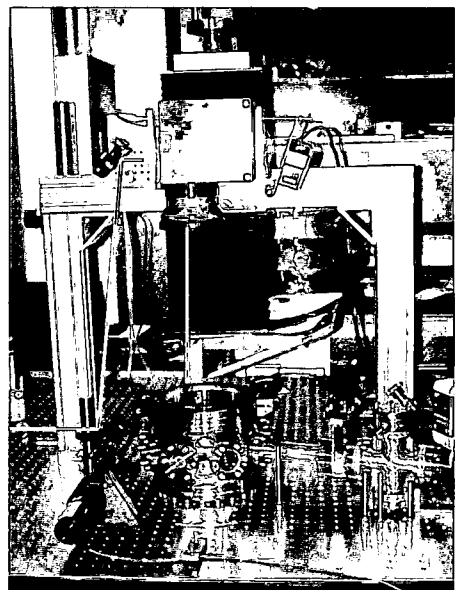
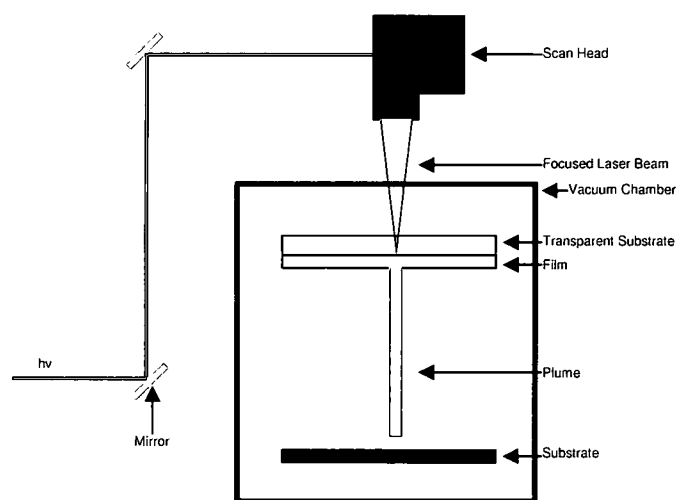


Figure 4.1. Illustration and picture of the experimental setup and equipment, with the beam path shown.

4.2 – Measurement Techniques

Three main measurement techniques were used to characterize the plume constituents. The first consisted of a photomultiplier tube (PMT) set up to view the plume created from TTFA orthogonally to the direction of travel. By limiting the field of view of the PMT with a small slit, 2 mm in width, the amount of light detected by the plume over time would show the speed of the material as a function of the distance between the target and the slit. This distance was constant at 5 and 20 mm. The PMT was biased with a voltage of 900V, well below saturation. A schematic of the setup is shown in Figure 4.2.

The PMT signal was read by an oscilloscope. The oscilloscope was a LeCroy WaveRunner 6100A, which has a bandwidth of 1 GHz. The PMT was a Hamamatsu R928, with a wide spectral response from 185 nm to 900 nm, which includes the visible range, ensuring that what can be seen with the human eye will be captured by the PMT.

A second set of measurements consisted of recording the net charge of the plume over time for various conditions. A metal plate was electrically isolated inside the chamber and placed at a distance of both 5 and 20 mm below the target, as shown in Figure 4.3. The metal plate was connected via an uncoated wire to the oscilloscope, such that any ion striking the plate would change the electrical charge of the plate relative to the ground of the oscilloscope. The background pressure was kept constant at 13.33 Pa of argon.

A third set of measurements consisted of using an optical camera to record the temporal evolution of the emitting materials in the plume. The camera was a Princeton Instruments PI-MAX Intensified CCD, with a gating capability of less than 2 ns. By utilizing specific gate delays from the laser pulse trigger, the plume development can be seen as a collection of images for various conditions. The gate width was kept constant at 100 ns, and the camera gain was unchanged for all of the images. For each set of conditions, an image with a gate delay of 25 ns, 50 ns, 100 ns, 200 ns, 500 ns, 1 μ s, 5 μ s, 10 μ s, 20 μ s, 50 μ s, 100 μ s, 150 μ s and 200 μ s after the laser pulse was captured.

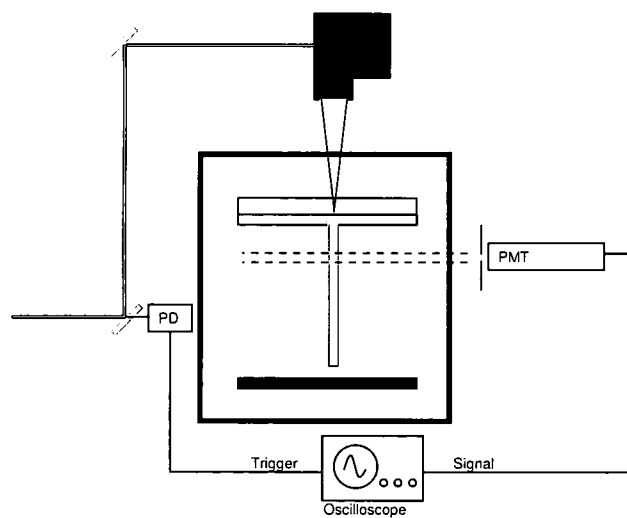


Figure 4.2. A schematic illustration of the setup with the plume being observed by a PMT.

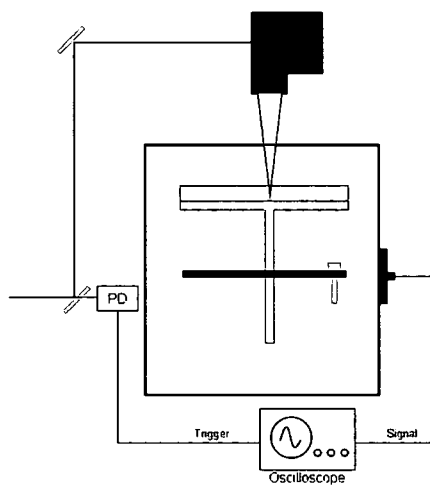


Figure 4.3. Schematic of the metal plate setup.

4.3 – Preliminary Experimentation

In developing the preliminary parameters for TTFA of an iron film, the location of focus of the laser was adjusted to vary the energy density of the laser at the target. Two different conditions were tried; the first was with the laser focus at the film, which resulted in an elliptical spot approximately 100 by 150 μm and an energy density of 1.01 J/cm^2 . The laser focal point was then lowered to a distance of approximately 5 mm below the film, with all other conditions remaining the same, which created a spot size of approximately 200 by 240 μm and an energy density of 0.34 J/cm^2 . Figure 4.4 (a) shows a schematic representation of the setup with the laser focus at the film, and Figure 4.4 (b) shows a representation of the setup with the laser focus below the film.

In studying the resultant particles from each ablation setup, it was seen that there were two different realms of particle formation. The first, from when the focus of the laser is at the film, gave very small, round particles, as shown in the SEM micrograph of Figure 4.5. The particles were clearly separated, and the high circularity of the particles implies that they were largely spherical in shape.

However, in examining the target after ablation, damage to the film substrate was evident. As can be seen in the three dimensional image produced with height data from the white light interferometer, the film was cleanly removed from the transparent support, but a deep well appeared in the center of the ablation spot, showing that the support was damaged in the ablation as well, which introduces contaminants into the particles. As the support substrate is composed of quartz, the containments are likely silicon, which can be problematic in some applications. Figure 4.6 shows the damaged area of a spot indicated with an arrow.

When the focal point of the laser was lowered to approximately 5 mm below the film, the resultant particles remained small and separated, but no longer appeared as round, or spherical, particles. The larger particles shown below in the micrograph of Figure 4.7 appeared to have struck the substrate while in a liquid form, creating shapes that appear as frozen splashes. This indicates that these particles were likely very thin and clearly had larger diameters than the particles formed with the laser focused at the film. While this might indicate the particles formed

with the laser focused at the film were smaller in diameter, the likely difference in thickness indicates that the particles from each set of conditions contained approximately the same volume of material.

Examining the target after ablation, however, shows that the central damaged region was not evident when the laser focal point was below the film. The height data from the white light interferometer show that the film was removed, as seen in Figure 4.8. The reddish area is the region with removed material, and this area does not vary in thickness across the surface.

It is counterintuitive that a setup with a higher laser energy density would produce particles that appear to be solid when deposited onto the surface, while a lower energy density produces liquid particles, as more energy is necessary to melt the target. In either case, while TTFA has been shown to create small, separated nanoparticles, there is not an effective understanding of the effects of changing the location of the laser focus. In changing this single parameter, two different effects were seen in both the target and the particles. These changes are hypothesized to be due to the dynamics of the formation of the plume. This will be examined further and an understanding of the dynamics of the plume formation and the effect on the resultant particles will be presented.

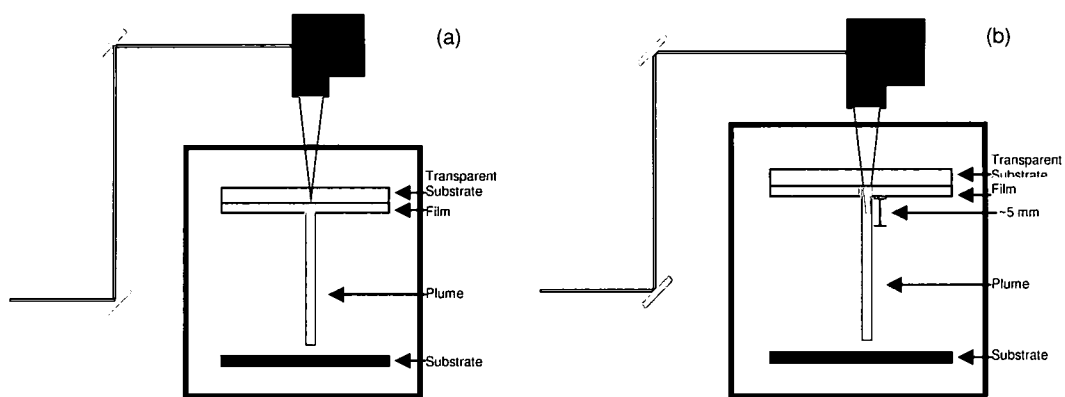


Figure 4.4. Schematic drawings of each setup, with the vacuum chamber, scan head, target, plume and substrate shown. (a) shows the setup with the laser focus at the film, while (b) is with the laser focus ~5 mm below the film.

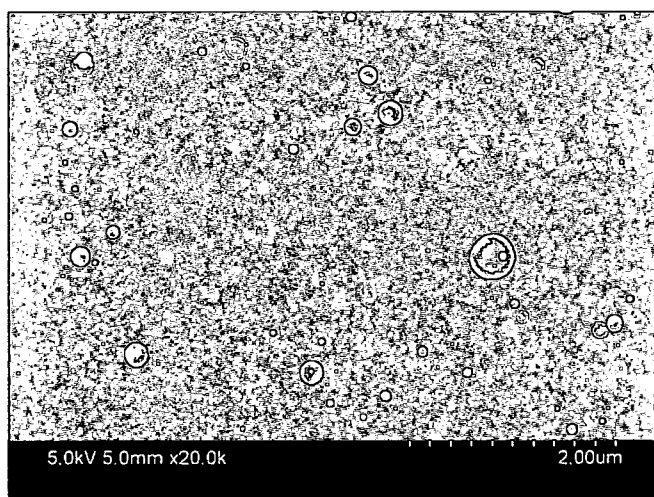


Figure 4.5. SEM micrograph of particles formed with the laser focus at the film. The particles appear separated and spherical. The scale bar is 2.00 μm .



Figure 4.6. White light interferometer data of an ablated spot. The damaged region in the center is indicated with an arrow.



Figure 4.7. SEM micrograph of particles formed with the laser focal point approximately 5 mm below the target film. An example of a particle that appears to have struck the surface in a molten form is indicated with a white arrow. The micron bar is 2.00 μm .

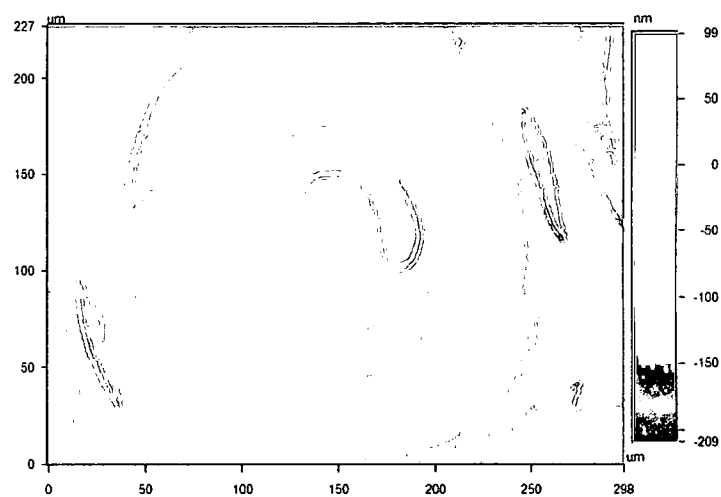


Figure 4.8. White light interferometer data showing the removed film, in the reddish area, from the substrate. No area of damage to the substrate can be seen.

CHAPTER 5

RESULTS

5.1 – PMT Measurements and Speed Calculations

The first set of measurements was to measure the speed of the plume under various conditions by setting up a PMT with a slit to limit the field of view, as shown in Figure 5.1.

While previous work has indicated that thinner films create smaller particles, a film thickness needed to be chosen that would show the greatest intensity of light detectable by the PMT. Using identical conditions, two films were ablated with the laser focus set at the film and the PMT set 5 mm below the target. As can be seen in Figure 5.2, the intensity of the 10 nm film is greater than the 25 nm film, which would provide a better standard for the experimentation.

For all PMT measurements, regardless of setup, distance or pressure, the time for the intensity to return to 0 was significantly long, as shown in Figure 5.3. Here, for example, the viewing distance was 5 mm in a pressure of 13.33 Pa with the focal point of the laser at the target, and the intensity did not return to zero until approximately 50 μ s after the laser pulse. However, the intensity appeared to be uniformly distributed throughout this time, indicating that there are no events within the plume, and as such the time scales have been shortened in all of the following plots to focus on the events in the temporal regions of interest.

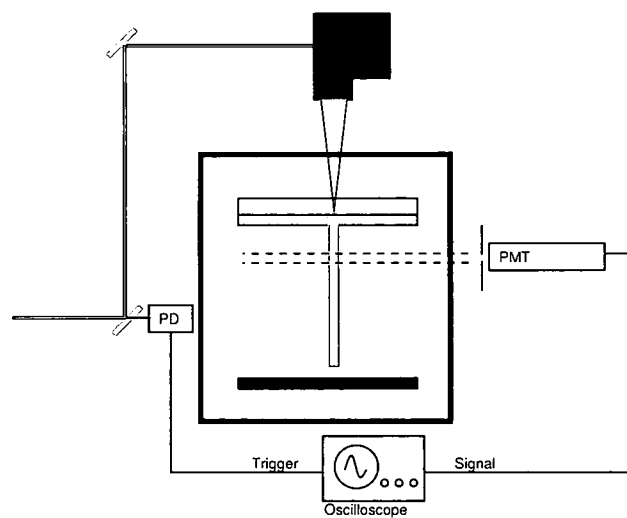


Figure 5.1. A schematic illustration of the setup with the plume being observed by a PMT.

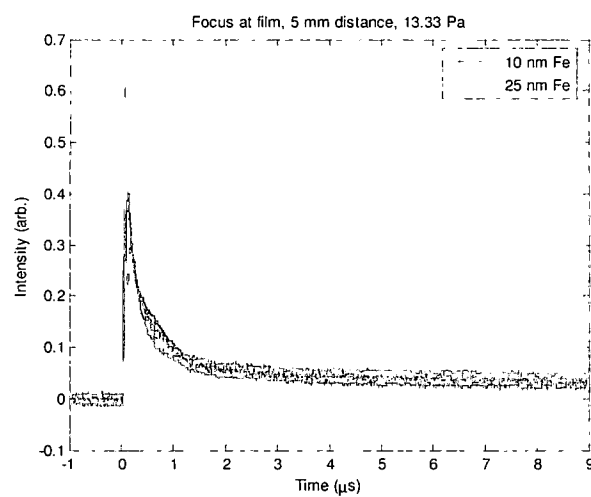


Figure 5.2. Plot of the intensity of the plume for both a 10 nm iron film (blue curve) and a 25 nm iron film (green curve). The intensity of the 10 nm iron film is greater.

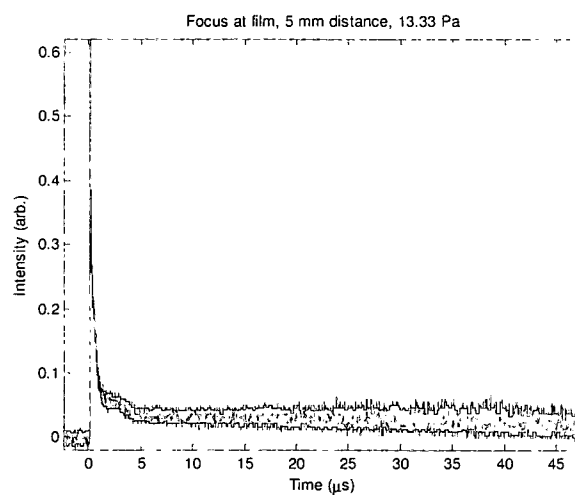


Figure 5.3. Plot of the PMT signal over a long time interval, showing the gradual return of the intensity to 0.

5.1.1 – PMT Measurements with the Laser Focus at the Target

In keeping the laser focus at the target, a range of pressures were examined to see if a background pressure of argon would vary the plume formation. For an initial measurement, an ablation was measured in vacuum, with the PMT slit 5 mm below the target surface. The resultant plot, shown in Figure 5.4, shows a sharp initial peak, followed by a relaxation in intensity and a second peak following approximately 142 ns later. The first peak is the laser striking the film, while the second peak appears to be material traveling in front of the PMT. Using the time delay and the 5 mm distance to the viewing area, a speed of 35.3 km/s was found for the material. For this and all measurements with the laser focus at the target, no evidence of any peaks was found at longer timescales.

Increasing the pressure to 1.33 Pa showed a similar result in Figure 5.5. The second peak was better defined and appeared sharper. Using the same calculations, a speed of 53.6 km/s was found for the material, significantly greater than for the ablation in vacuum.

Increasing the pressure of argon to 13.33 Pa continued to show the first peak from the laser, as well as a very small second peak and larger third peak from the material. A fourth peak was also evident, seen as a shoulder of the third peak, occurring approximately 650 ns after the laser pulse. Figure 5.6 shows this peak as a change in inflection of the curve of the tail of the intensity signal. The speeds of each peak are shown in the plot, with a speed of 140.5 km/s for the second peak, 57.3 km/s for the third peak and a speed of 7.5 km/s for the fourth peak. This shows that the speed for the third peak has remained constant in increasing pressure from 1.33 to 13.33 Pa.

Increasing the pressure to 66.66 Pa continued to show the same three peaks, although they appeared sharper and better defined than at lower pressures. Figure 5.7 shows the plot of the signal, with the speed of the second peak at 79.0 km/s and the speed of the third peak at 13.3 km/s. Both of these speeds are significantly faster than the speeds at lower pressures. Increasing the pressure further only served to squash the entire signal detectable by the PMT.

Changing the viewing distance to 20 mm below the target did not show any peaks in intensity, either in vacuum or in 1.33 Pa of argon. As can be seen in Figure 5.8, only the initial

laser peak can clearly be seen, with a trailing off of intensity as the material moves in front of the PMT. There did not appear to be any defined groups of material, and only tapering distribution of material at the farther distance.

Increasing the pressure to 13.33 Pa showed distinct second and third peaks, at a speed of 502.5 km/s and 36.6 km/s, respectively, as seen in Figure 5.9.

By increasing the pressure further to 66.66 Pa of argon, three distinct peaks, in addition to the laser peak, were seen as shown in Figure 5.10. The second and third peaks appeared as changes in the slope of the signal, while the first peak appeared as a sharp peak closely following the laser peak. The speeds for the three peaks are 512.8 km/s, 57.2 km/s and 14.8 km/s, respectively.

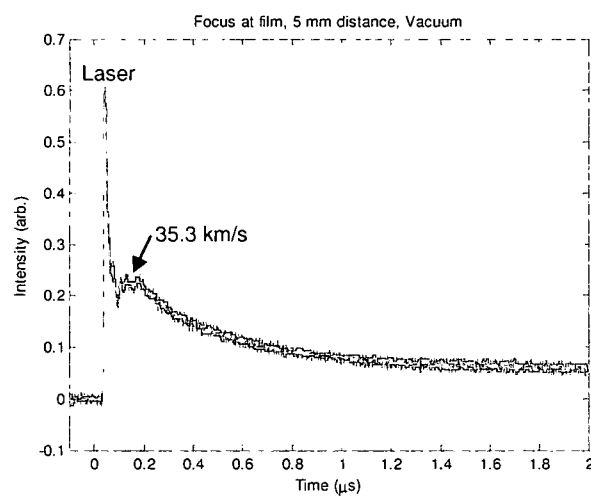


Figure 5.4. PMT signal from an iron film ablated in vacuum with the laser focus set at the film.

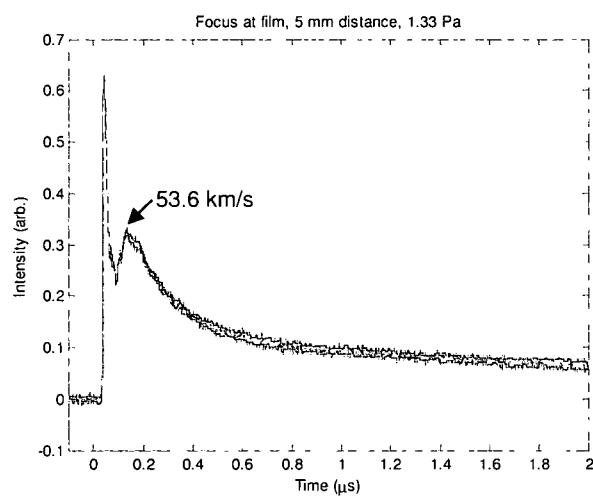


Figure 5.5. Ablation in 1.33 Pa of argon.

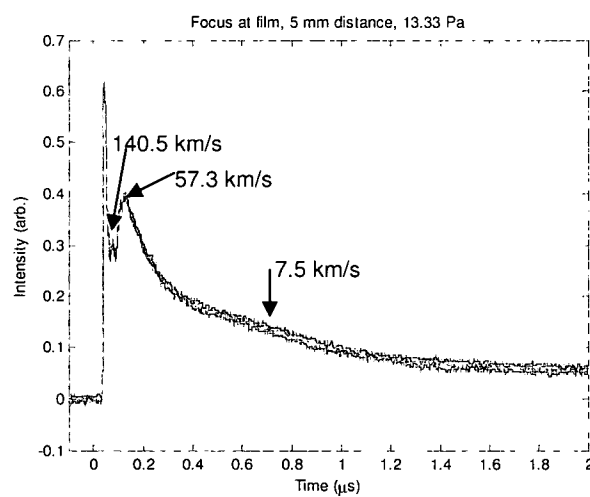


Figure 5.6. Ablation in 13.33 Pa of argon. Note the third peak that appears as a change in the slope of the curve.

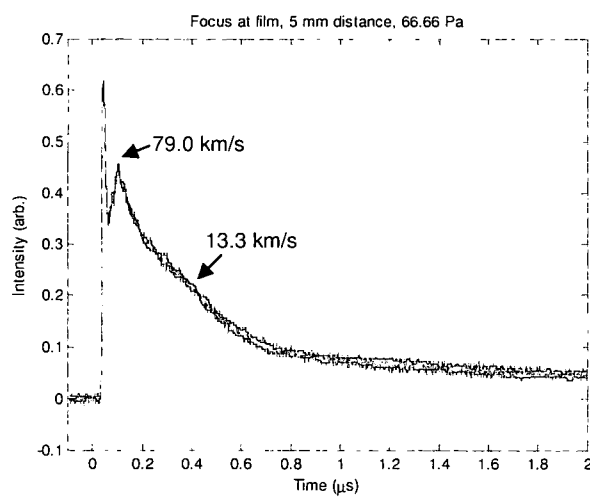


Figure 5.7. Ablation in 66.66 Pa of argon.

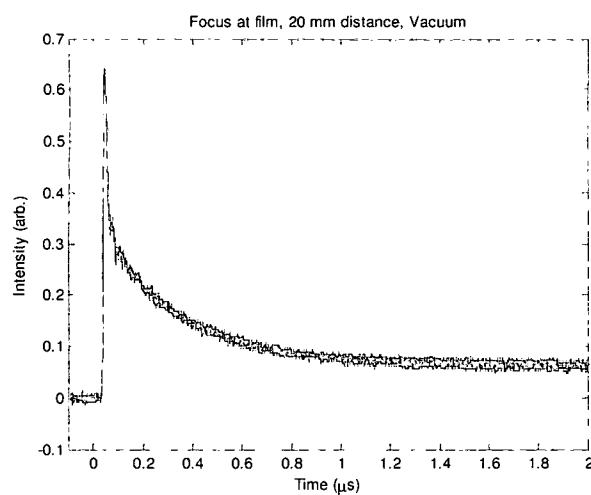


Figure 5.8. Ablation in vacuum at a distance of 20 mm. No distinct peaks, other than the laser peak, can be seen.

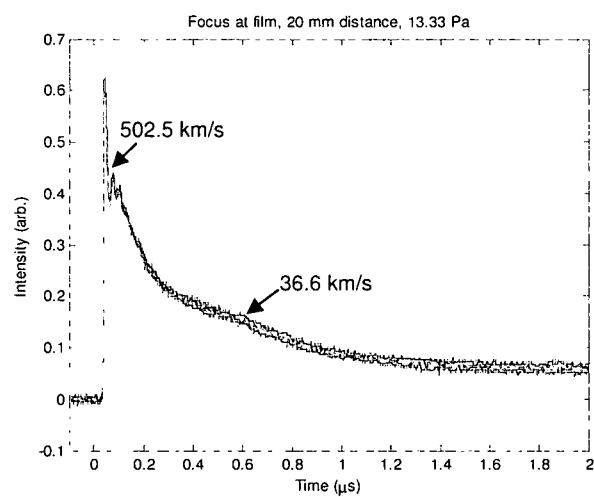


Figure 5.9. Ablation with a distance of 20 mm in 13.33 Pa of argon.

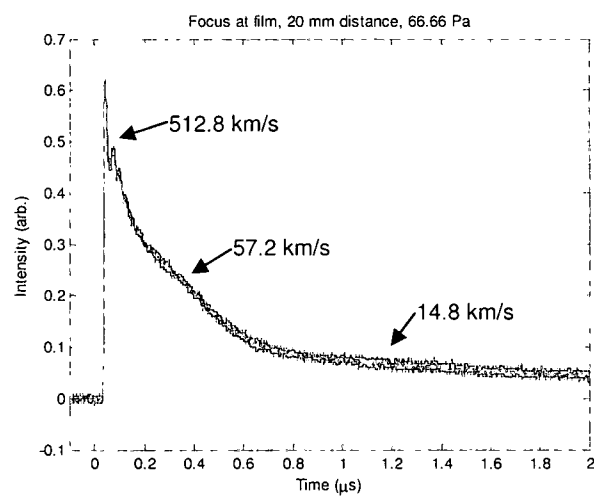


Figure 5.10. Ablation in 66.66 Pa of argon at a distance of 20 mm.

5.1.2 – PMT Measurements with the Laser Focus below the Target

Changing the location of the laser focus relative to the film showed significant differences in the signal detected by the PMT. The focal point of the laser was lowered to a location approximately 5 mm below the target, and the distance between the film and the viewing region of the PMT was held constant at 5 and 20 mm. This setup can be seen schematically in Figure 5.11.

At a viewing distance of 5 mm, the same range of pressures was tried as with the laser focus at the film. As can be seen in Figure 5.12, adjusting the laser focus gave a very small peak about 8 μ s after the laser peak. This results in a speed of 803.0 m/s, significantly slower than any peak seen with the laser focus at the film. Looking at the shorter time durations, only a steady decay of the intensity is seen in Figure 5.13.

Increasing the background pressure of argon to 13.33 Pa also did not show a change in intensity in the shorter time scale. However, as seen in Figure 5.14, a very faint peak was seen, comparable to the ablation in vacuum, with a speed of 781.6 m/s.

Increasing the distance between the target and the PMT to 20 mm did show some slight differences. While no peaks were found in the shorter time region, a peak was evident at a speed of 7.7 km/s for the ablation in vacuum, while a peak with a speed of 15.2 km/s was found in the ablation with 13.33 Pa of argon. These are shown below in Figures 5.15 and 5.16.

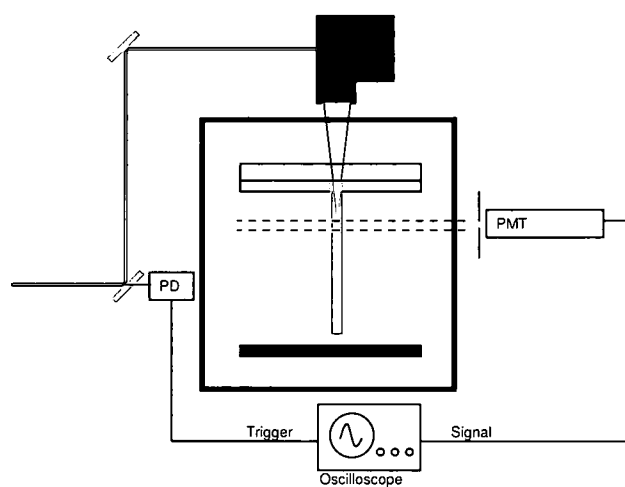


Figure 5.11. Schematic illustration of the setup for the PMT collections with the laser focus below the film.

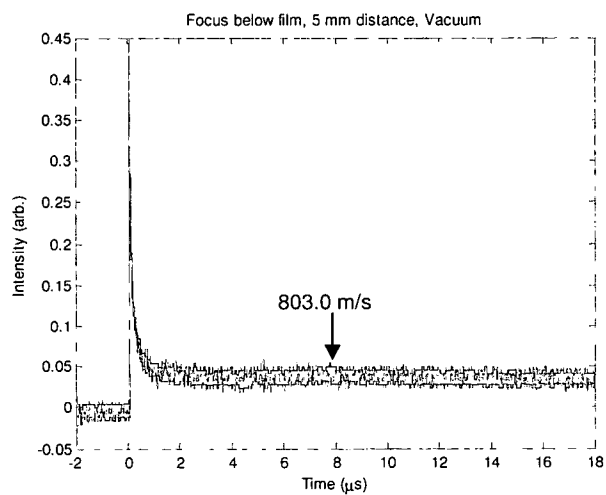


Figure 5.12. Ablation in vacuum with the laser focus below the film.

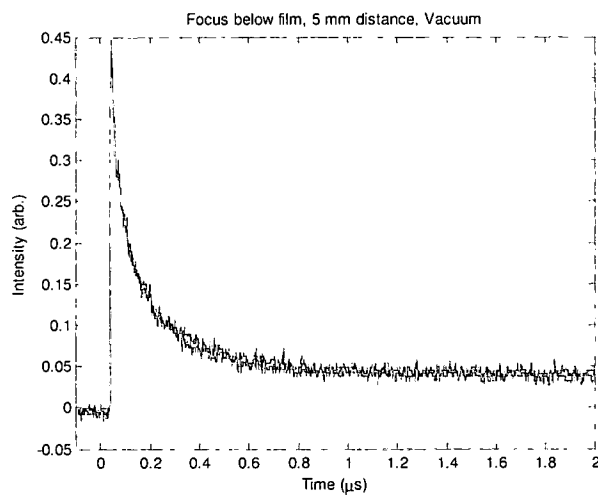


Figure 5.13. Looking at the shorter time delay, no significant changes in intensity are seen.

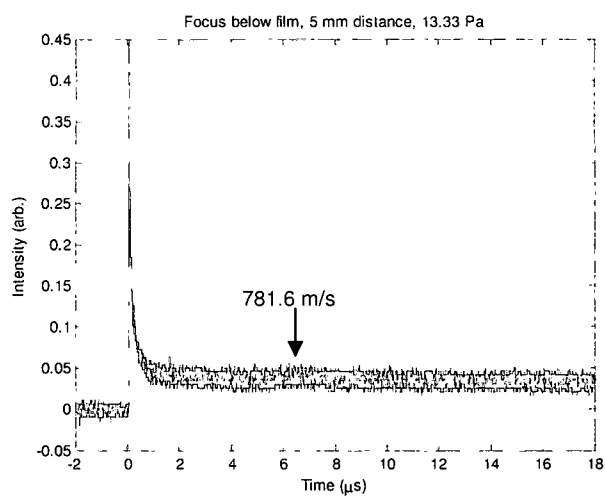


Figure 5.14. Ablation in 13.33 Pa of argon.

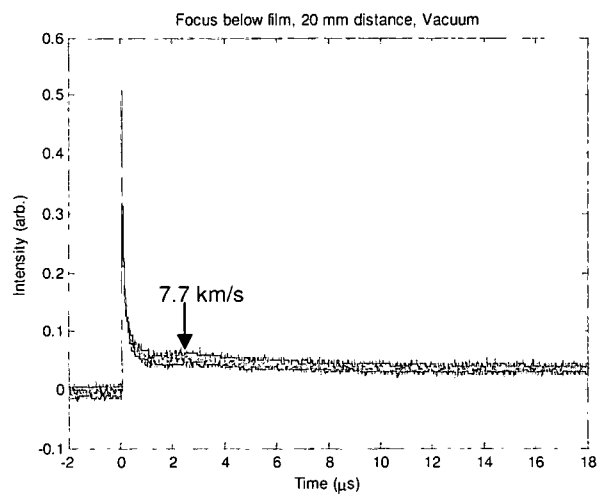


Figure 5.15. Ablation viewed at a distance of 20 mm in vacuum.

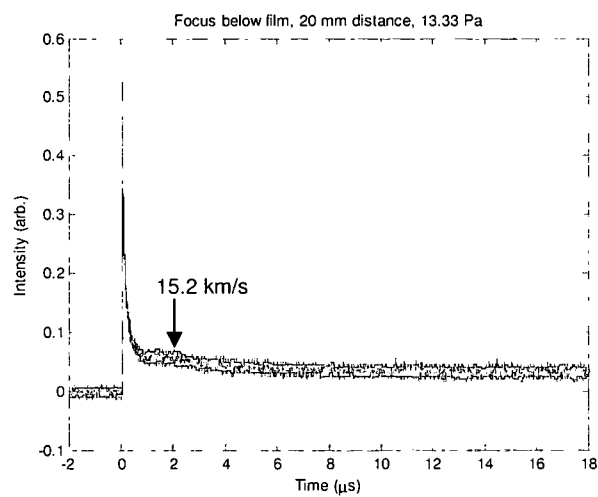


Figure 5.16. Ablation in 13.33 Pa of argon.

5.2 – Charge Plate Measurements

While the speeds of the peaks appeared dramatically different for each setup of the laser focus, more information on the plume itself was necessary to characterize this process. A metal plate was electrically isolated to measure the net charge of the plume, as shown in Figure 5.17. The background pressure was kept constant at 13.33 Pa of argon, while varying the location of the laser focal point and the distance between the target and the charge plate. As before, these results were plotted with the charge measured in volts.

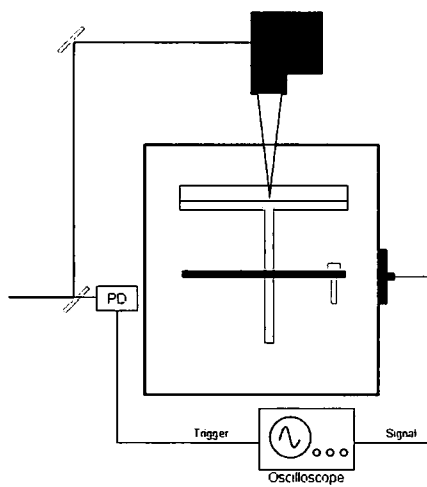


Figure 5.17. Schematic of the metal plate setup.

5.2.1 – Charge Plate Measurements with the Laser Focus at the Target

When the laser focus was set at the target and the metal plate was located 5 mm below the film, three distinct changes in the charge of the plate could be seen in Figure 5.18. There was a sharp initial spike that indicated the laser pulse, followed by a small negative dip, a strong positive peak, and a weaker negative dip. The speeds of each of these, relative to the laser spike, are 157.2 km/s, 31.2 km/s and 8.2 km/s.

Changing the distance to 20 mm increased peak width of the positive signal seen, and lowered the overall amplitude. The speed of the positive signal is 19.0 km/s, as shown in Figure 5.19.

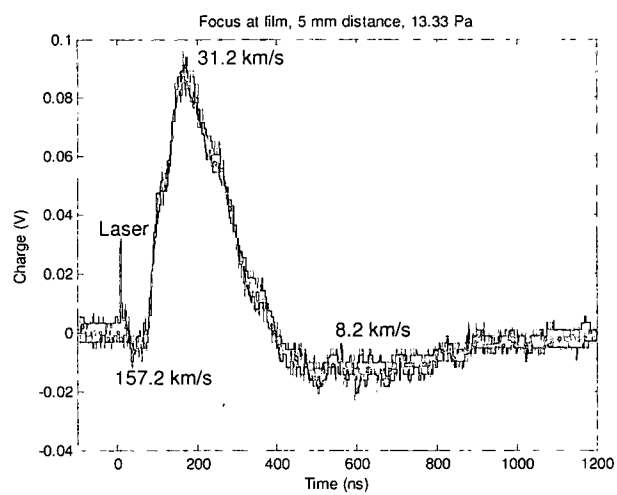


Figure 5.18. Plot of the charge of the metal plate with the laser focus at the film.

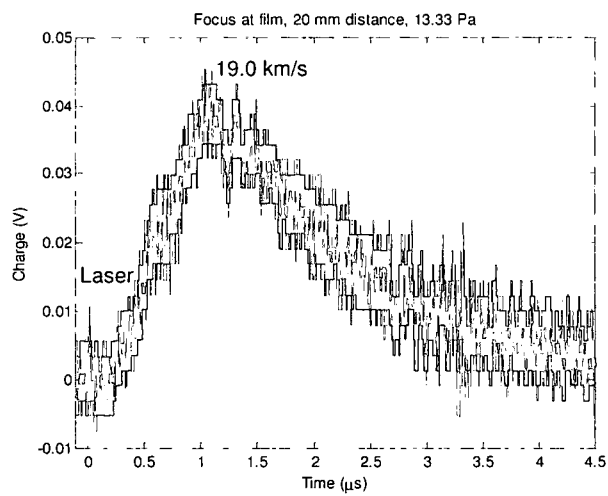


Figure 5.19. Plot of the change in charge of the metal plate at 20 mm distance.

5.2.2 – Charge Plate Measurements with the Laser Focus below the Target

Lowering the focal point of the laser to approximately 5 mm below the film significantly changed what is seen by the metal plate. As can be seen in Figure 5.20, at a distance of 5 mm the metal plate does not show a change in charge other than the initial laser spike. At a distance of 20 mm in Figure 5.21, not even the laser spike was seen.

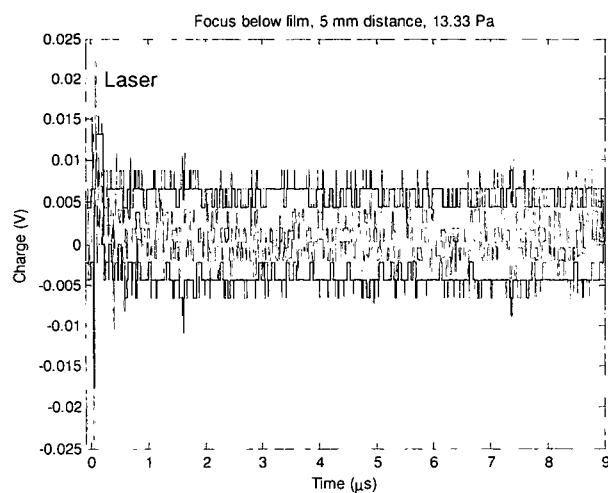


Figure 5.20. Signal from the metal plate at a distance of 5 mm.

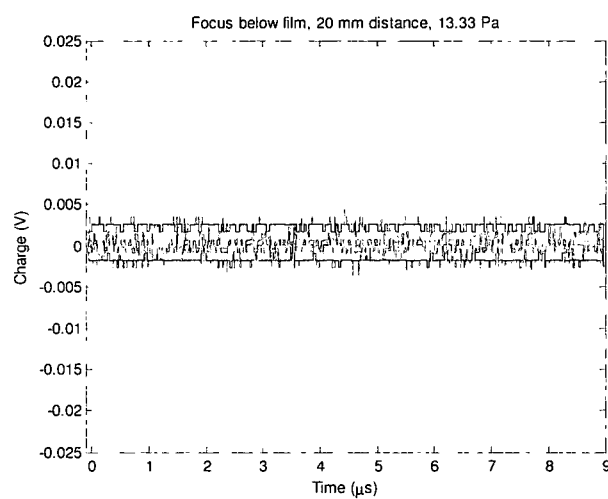


Figure 5.21. Signal from the metal plate at a distance of 20 mm.

5.3 – Optical Images of the Ablation

To try to better visualize the temporal evolution of the plume, a gated intensified CCD camera was used to capture the plume formation at specific gate delays from the laser pulse trigger. The laser focus was set both at the target and 5 mm below the target in a variety of background pressures. The camera was oriented such that the plume appears to travel from the right side of the image to the left. A sample, with the target and substrate indicated, is shown in Figure 5.22. The distance between the target and the left side of the image is approximately 36 mm.



Figure 5.22. A sample image, showing the target and substrate for the purpose of illustration.

5.3.1 – Optical Images with the Laser Focus at the Target

With the laser focused at the film and in a vacuum environment, a series of images were captured at various time delays. As can be seen in Figure 5.23, a plume appeared 25 ns after the trigger, left the target and traveled approximately 15 mm before completely dispersing at 1 μ s after the trigger. By 5 μ s, a second plume had formed, traveled towards the substrate while dispersing material, and relaxed to not emit light prior to 100 μ s.

At a pressure of 1.33 Pa, the plumes appeared much better defined, showing clearer edges and more emitting material. As can be seen in Figure 5.24, the first plume remained compact for the first 500 ns of travel, and while it did disperse in a large cloud, was evident up to 5 μ s after the trigger. The second plume took longer to disperse, remaining evident after 100 μ s.

At a higher pressure of 13.33 Pa, the plumes remained well defined, but did not travel as far as in 1.33 Pa of argon. Figure 5.25 shows the temporal evolution of the plume, which showed the same, well defined plume boundaries as before, but in looking at the images from the 1 μ s delay and the 5 μ s delay, one can see that the first plume has not travel significantly further towards the substrate in the interim time. There was also very little of the second plume evident after 50 μ s.

At a background pressure of 66.66 Pa of argon, the images indicated that there were two separate plumes, but neither plume appears to have left the target surface. As can be seen in Figure 5.26, both plumes appeared wider, neither appeared to disperse towards the substrate, and both remained on the target surface without traveling towards the substrate. The second plume was still evident at 50 μ s, but it is interesting to note in the 20 μ s delayed image the short, higher intensity central region of the plume, with some dispersion around it, which had not been evident previously.

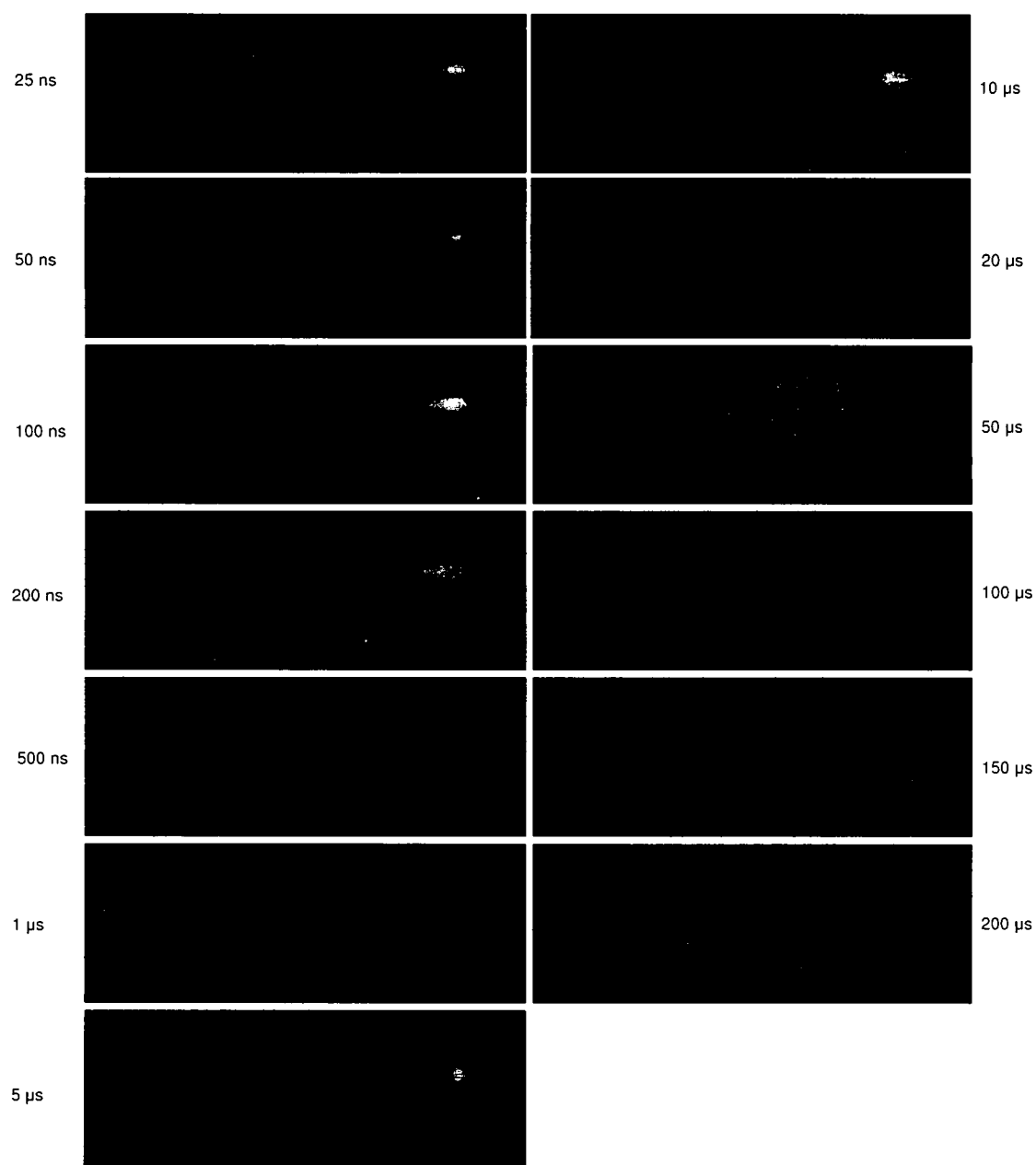


Figure 5.23. Images collected at various delays, labeled along the edge of the image, with the laser focus at the film and in a vacuum environment.

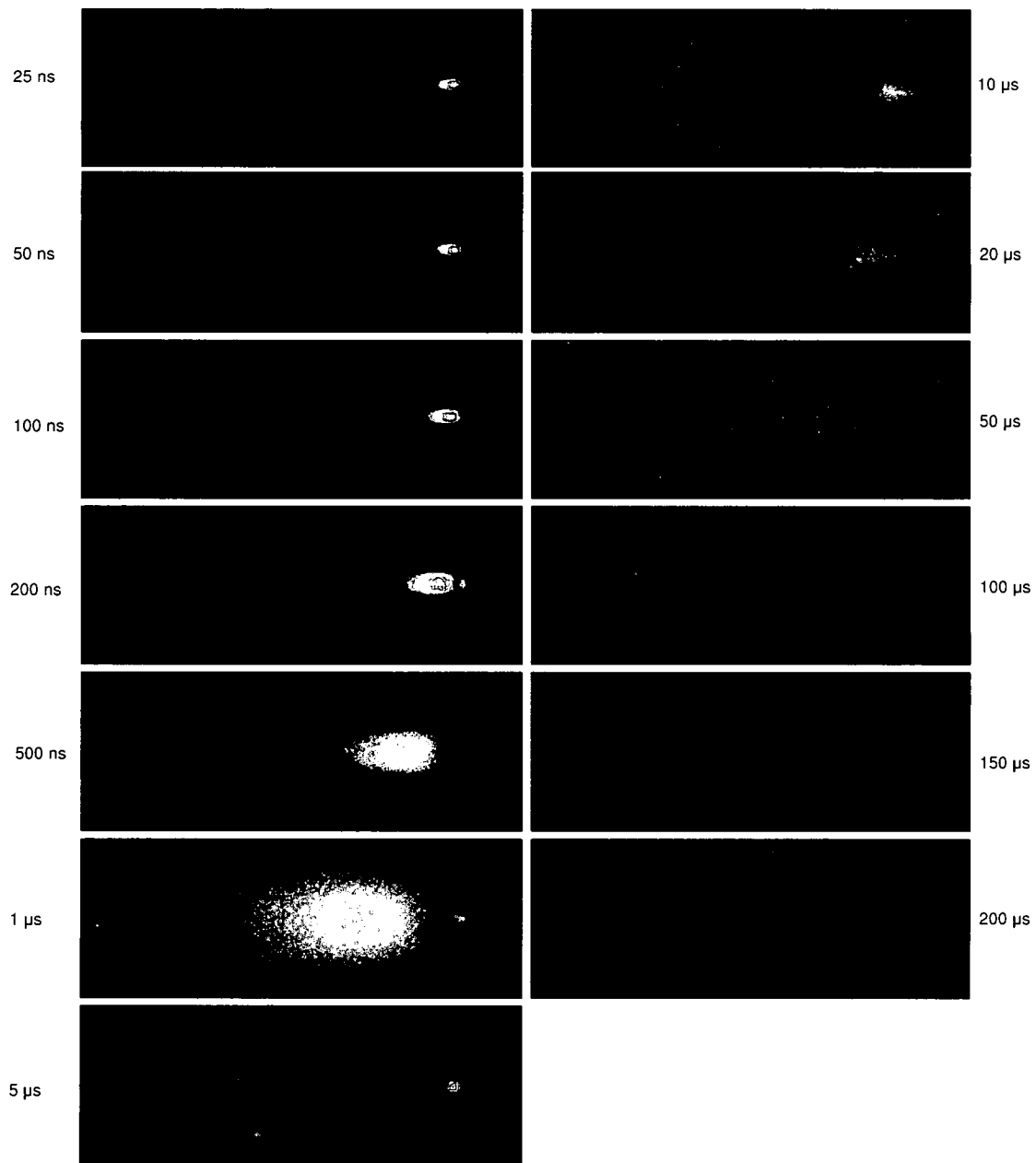


Figure 5.24. Images collected at various delays at a pressure of 1.33 Pa.

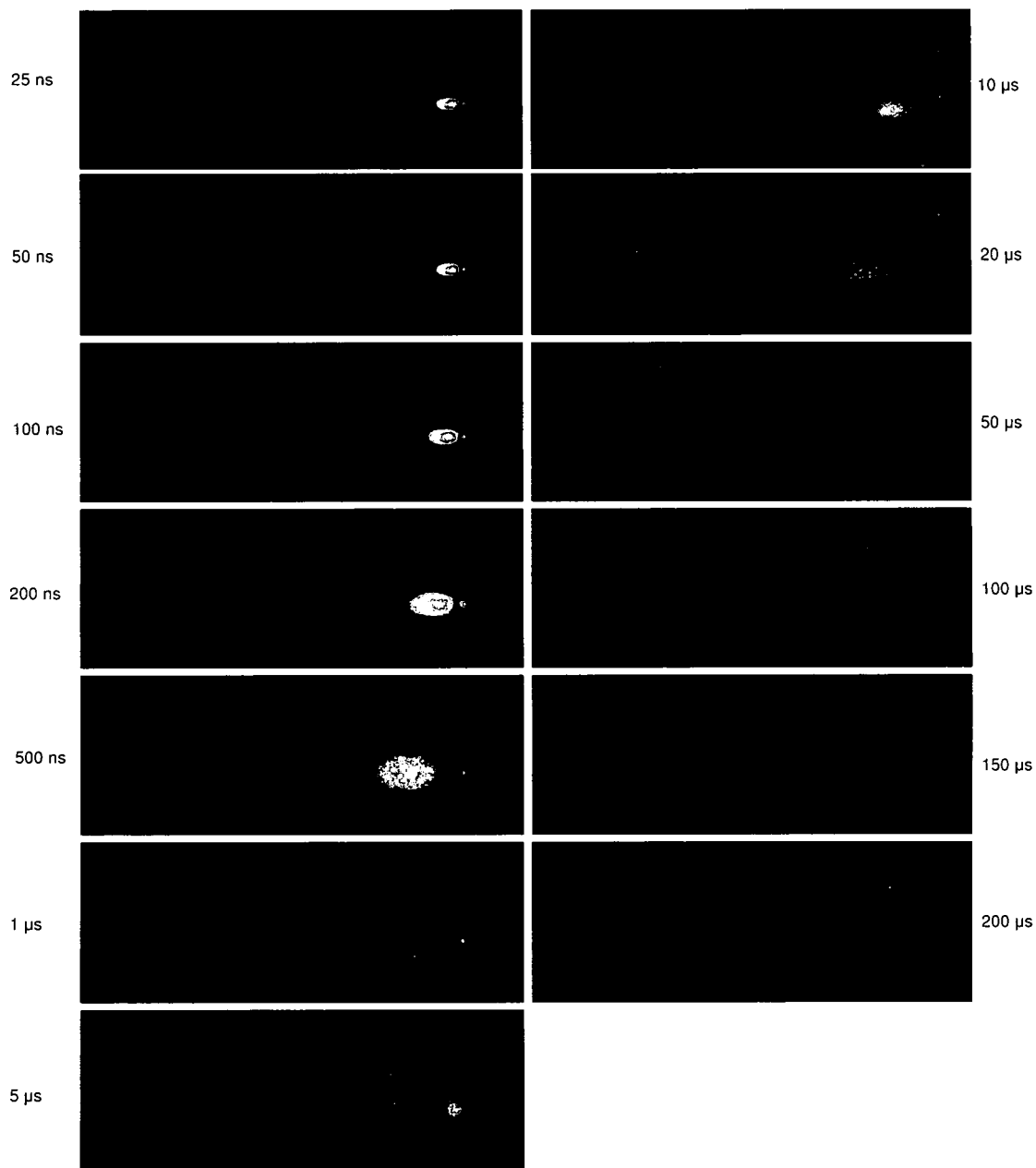


Figure 5.25. Images collected at various delays at a pressure of 13.33 Pa.

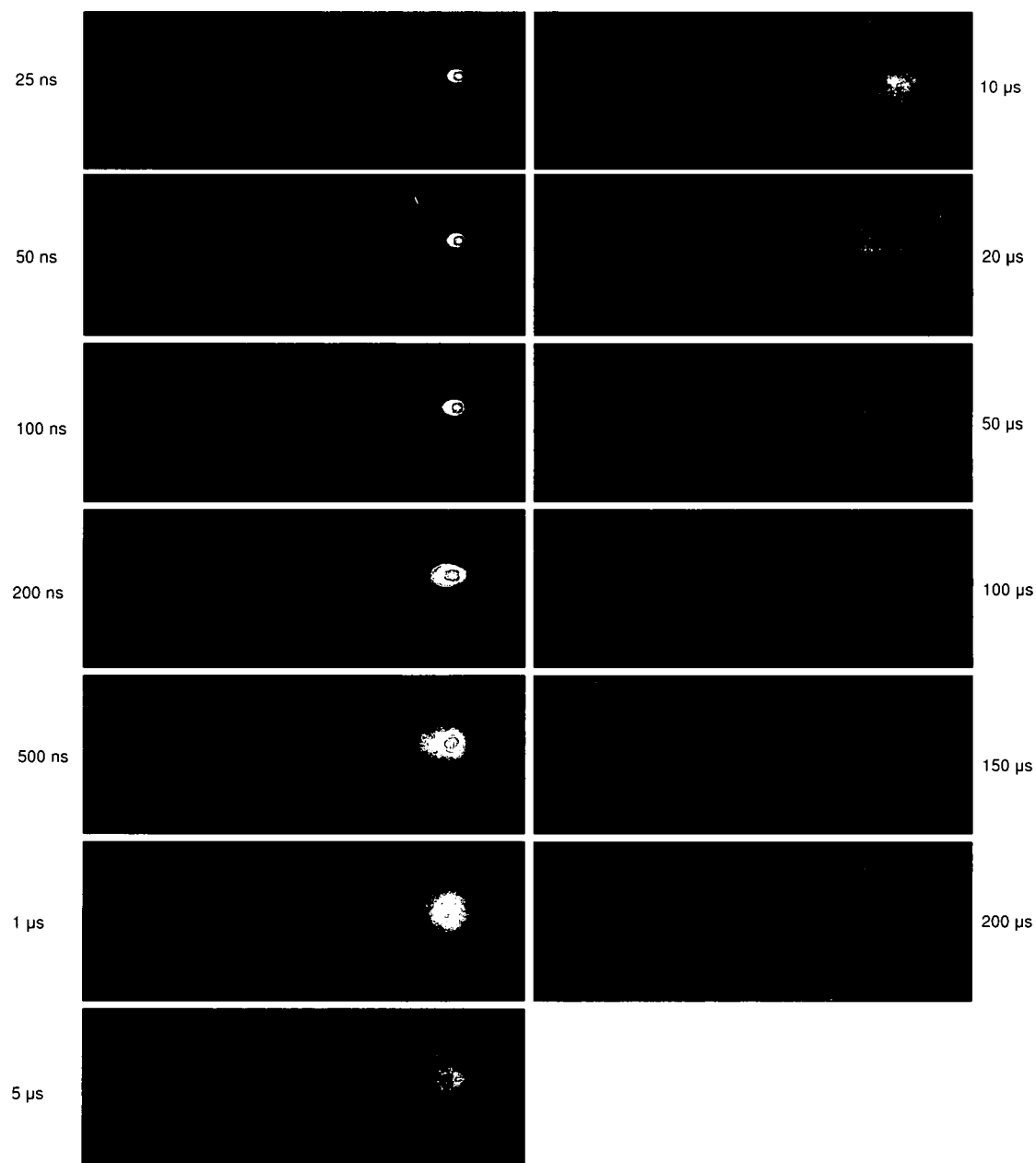


Figure 5.26. Images collected at various delays at a pressure of 66.66 Pa.

5.3.2 – Optical Images with the Laser Focus below the Target

In changing the location of focus, differences in the plume were evident when the laser focus was 5 mm below the target. Examining the plume in the same background pressures of argon showed that only one plume is formed, and that it took a long time, approximately 10 μs , to leave the target surface. As can be seen in Figure 5.27, obtained in a vacuum environment, only a glow from the target was visible for the first 500 ns after the trigger. A plume was seen 5 μs after the trigger, but still remains on the target surface, traveling out at 10 μs and fully dispersing towards the substrate by 150 μs .

In a background pressure of 1.33 Pa, there was no significant difference in the plume formation as compared to the plume formation in vacuum, as seen in Figure 5.28.

At a pressure of 13.33 Pa, the plume appeared brighter and more clearly defined, particularly at longer gate delays than 1 μs . As can be seen in Figure 5.29, the plume 5 μs after the trigger appeared significantly brighter and better defined, indicated by the bright center, and a dimmer leading edge of material. The plume also remained visible for longer, with a clearly defined area of material seen 100 μs after the trigger.

At a pressure of 66.66 Pa, the greater pressure of argon could be seen to affect the plume shape as it formed on the target surface. Looking at Figure 5.30, at the 1 μs delay, the plume could clearly be seen, but the leading edge did not appear round or cylindrical in shape. The leading edge formed a mushroom shape, more characteristic of a shock wave, due to the argon pressure pushing on the plume. However, at longer delays, the plume returned to the cylindrical shape seen previously.

Looking at the plume development and formation from the measurements of the intensity of light detected by a PMT, the charge of the plume as it strikes a metal plate, and gated camera images viewing the plume development over time, it is easy to see that there are noticeable differences in the plume formation depending on the location of the focal point of the laser. These differences will be discussed in further detail in the next section.

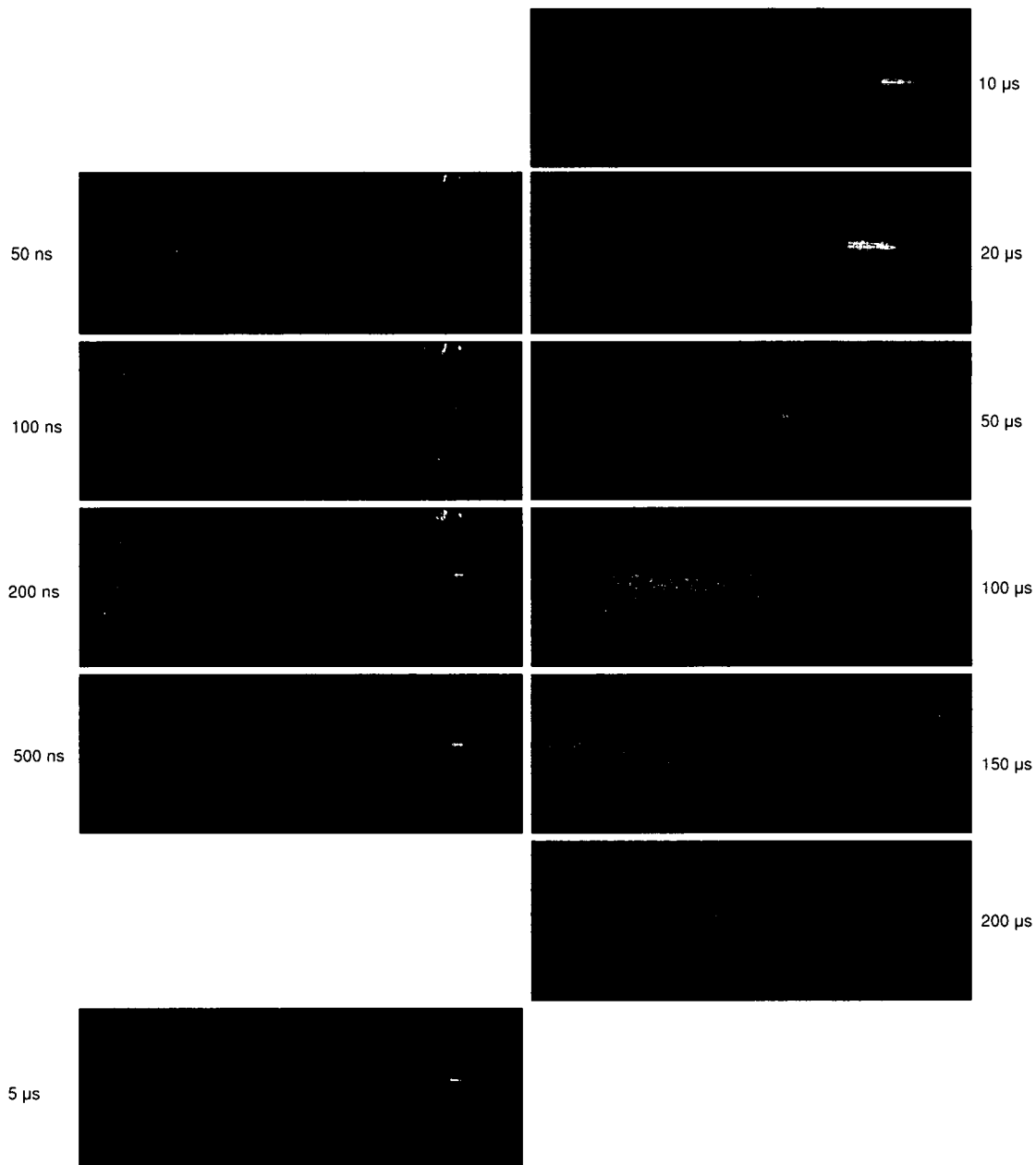


Figure 5.27. Images collected with the laser focus below the film in vacuum.

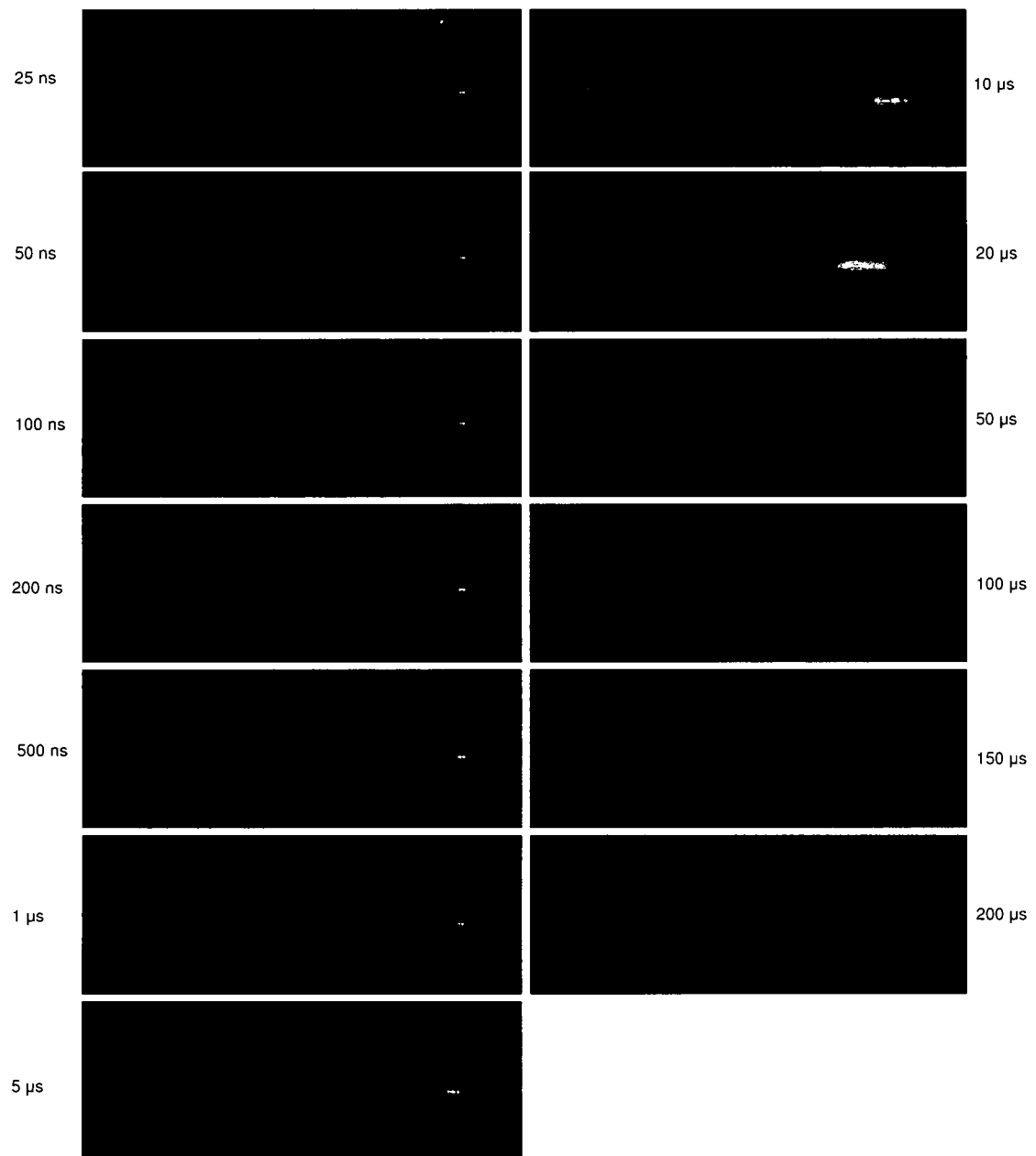


Figure 5.28. Images collected at various delays at a pressure of 1.33 Pa.

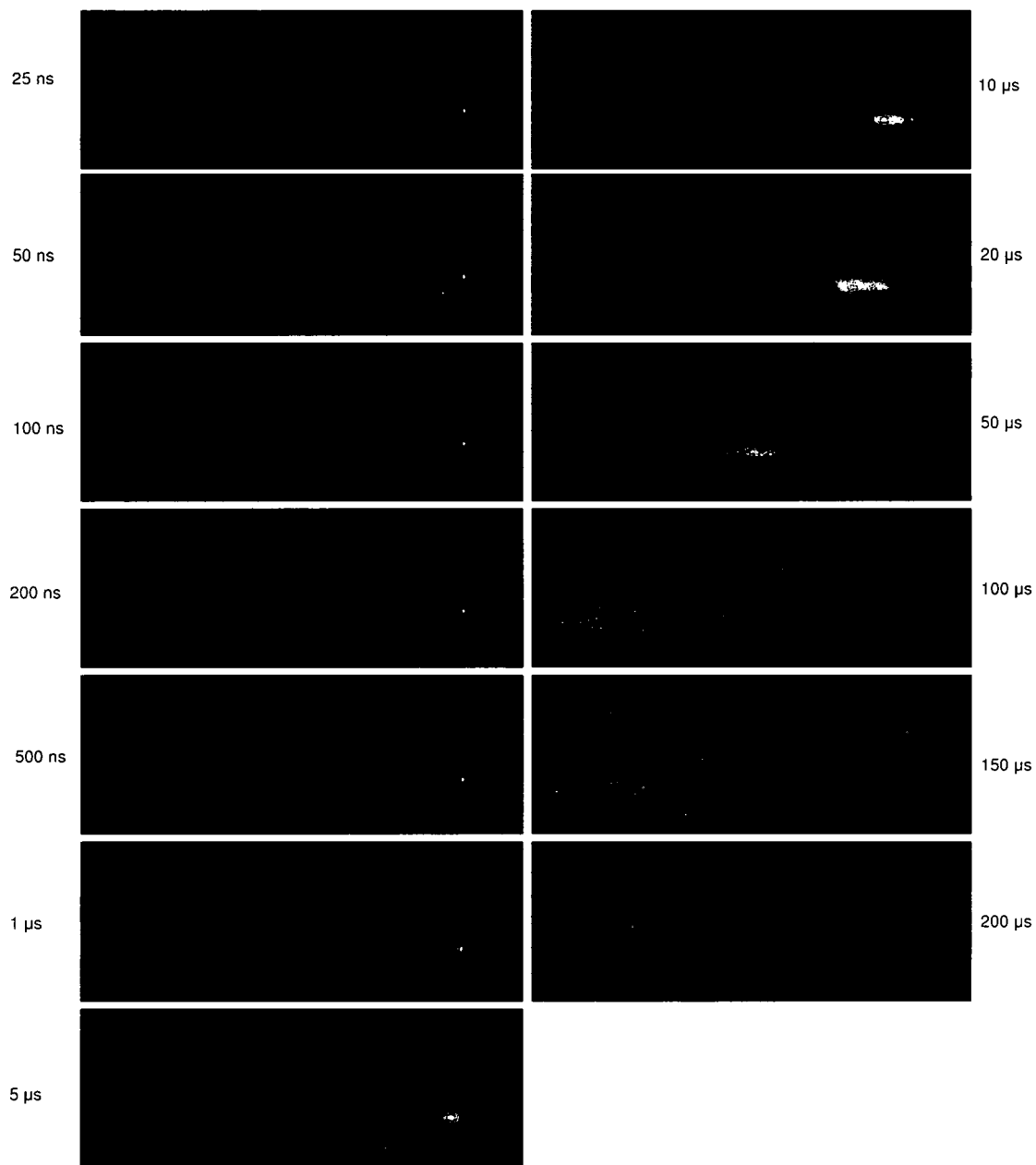


Figure 5.29. Images collected at various delays at a pressure of 13.33 Pa.

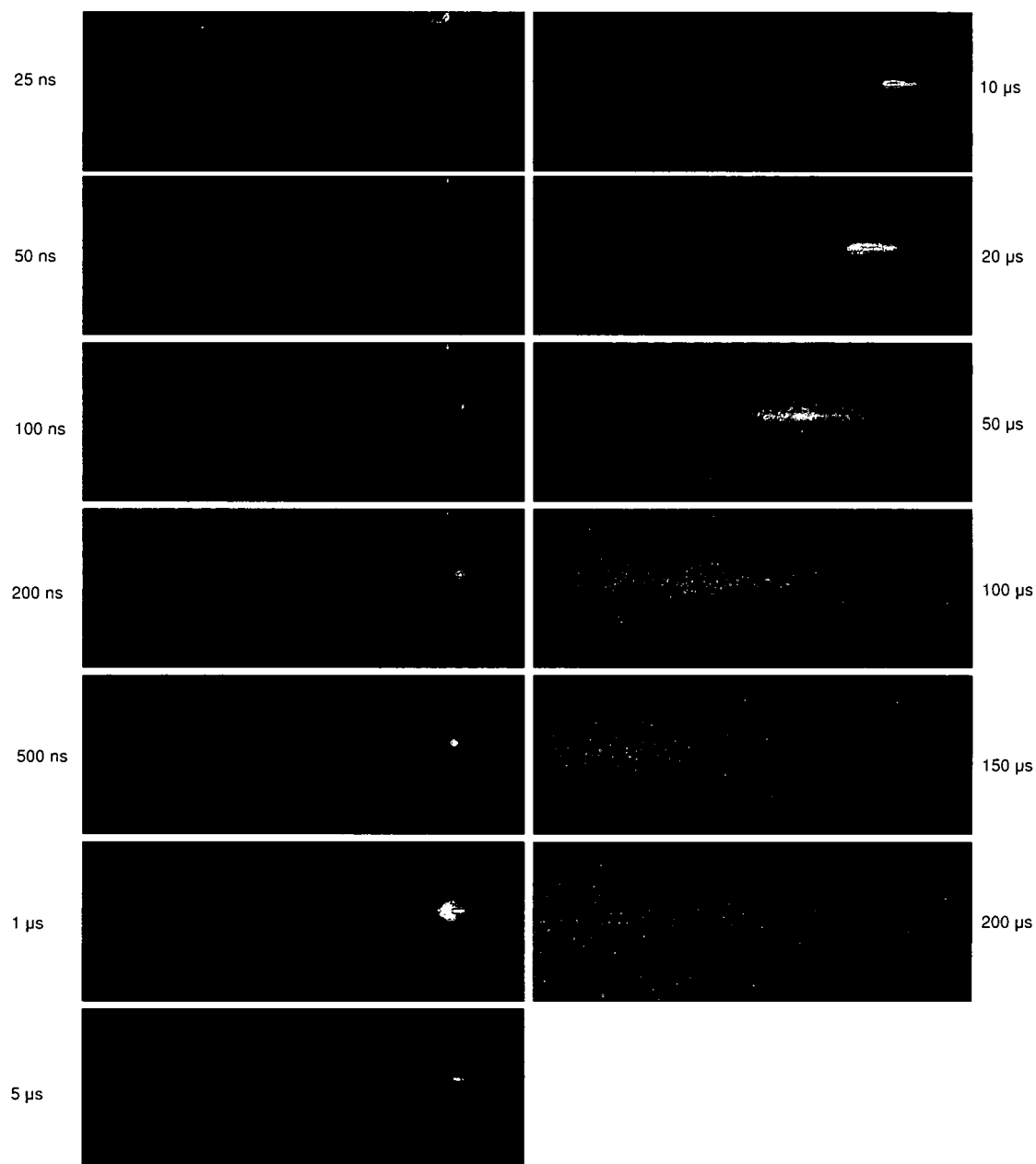


Figure 5.30. Images collected at various delays at a pressure of 66.66 Pa.

CHAPTER 6

DISCUSSION

In looking at the data presented, several factors had a significant effect on the plume formation. Varying the pressure of the background gas has a large effect, but varying the laser focal point created even more dramatic changes.

6.1 – Affect of Film Thickness and Background Pressure

6.1.1 – Affect of Film Thickness

It is easy to understand the effect of the film thickness on determining more measurable results. It was shown that a thinner target film (10 nm of iron) gave a stronger intensity of light as detected by the PMT than a thicker (25 nm of iron) film. This is due to the fact that the thinner film possesses less material for the same sized ablation area, while each laser pulse contains the same amount of energy. A thinner film would absorb the energy and, with fewer bonds to be broken to ionize the material, the energy would excite the atoms, causing more emission for detection.

6.1.2 – Affect of Background Pressure

Similarly, the increasing background pressure would allow for more interactions between the plume and the argon gas for the gated camera images. Regardless of other conditions, the plumes appeared brighter in higher levels of background gas as detected by the PMT, as the excited material would collide with the gas atoms, causing more emissions. However, increasing the pressure beyond a point would have adverse effects on the plume formation, by repressing the travel of the plume, as seen when the laser focal point was at the film, or by distorting the plume shape into a shock wave, as when the focal point was below the film.

Increasing the pressure also increased the intensity of the light detected by the PMT. As can be seen in Figure 6.1, the higher pressures correspond to greater intensity as well as

apparently faster speeds, indicated by looking at time to the first peak from the laser peak. While these speeds are relatively close, ranging from 35.3 km/s to 79.0 km/s, the increase is counterintuitive, as one would think that having more material to collide with in the background gas would slow down the plume. However, the PMT can only see the excited material as it relaxes and gives off energy in the form of light, and having a higher background pressure simply increases the probability that the plume will strike and excite an atom due to the increasing excitation cross section, creating more emissions for collection. The higher intensity allows the leading edge of material to be detected sooner, which appears as a faster speed.

This effect is not noticed, however, in the ablations with the laser focus below the target. In short time scales, a gradual decay from the laser pulse is evident, as seen in Figure 6.2, which shows an ablation in vacuum and 13.33 Pa of argon. This can be attributed to when the laser strikes the film, which has enough energy to heat the target such that it gives off visible light in the form of black body radiation. As the slit to limit the field of view of the PMT is outside of the vacuum chamber, the PMT is able to view an area wider than the slit width, which indicates that the PMT is able to see the light emitted from the film directly as the laser strikes it. While a background gas, this light could be reflected off the background gas molecules and into the PMT detector, this would not occur in a vacuum environment. The decay of the light intensity is due to the cooling of the target. The amount of heat deposited by the laser would not change with the gas pressure, which results in an identical decay of intensity in vacuum and 13.33 Pa environments.

It should be noted while higher pressures increase the intensity of the information available for collection; a maximum benefit is also evident. At a pressure of 66.66 Pa and higher, the plume begins to distort in shape and the pressure changes its behavior in regards to the path of travel. This is seen most clearly in the gated camera image from having the laser focus below the target at a pressure of 66.66 Pa, with a gate delay of 1 μ s, shown in Figure 6.3. The plume clearly forms a mushroom shape, rather than a directional cylinder. This is likely due to the interaction of the smaller nanoparticles, approximately 1 nm in diameter, with the background gas. As the particle strike the argon molecules, the iron has enough kinetic energy to shed an

iron atom from the particle surface. In a 1 nm iron particle, 54 atoms are present, each with a mass of 55.845 amu, for a total mass of 5.01×10^{-24} kg [52]. From the optical image, the leading edge is traveling at a speed of 3424.8 m/s, resulting in a kinetic energy of 183.3 eV, which is greater than the 66 eV necessary to extract an atom from the surface. The excess energy would likely excite the atom, which would emit photons as the atom relaxes, creating the rounded shape of the plume. The images taken under the same conditions, but with the laser focused at the target, indicate that the plume does not freely leave the target surface to travel to the substrate as easily as in ablations at lower pressures, and instead the shape of the emission appears more rounded and wider than previously.

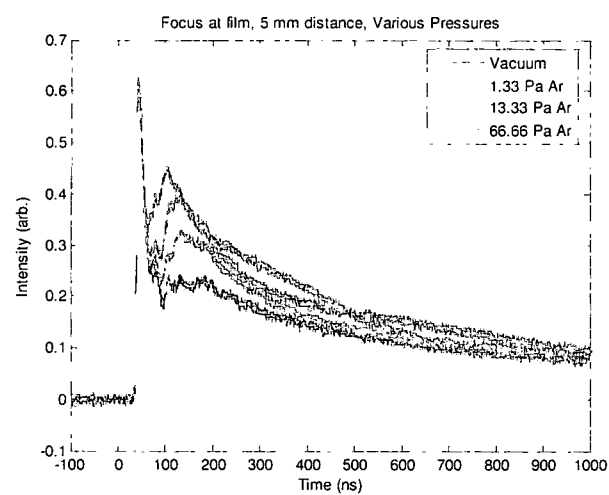


Figure 6.1. Signals captured by the PMT of the plume in various levels of background gas.

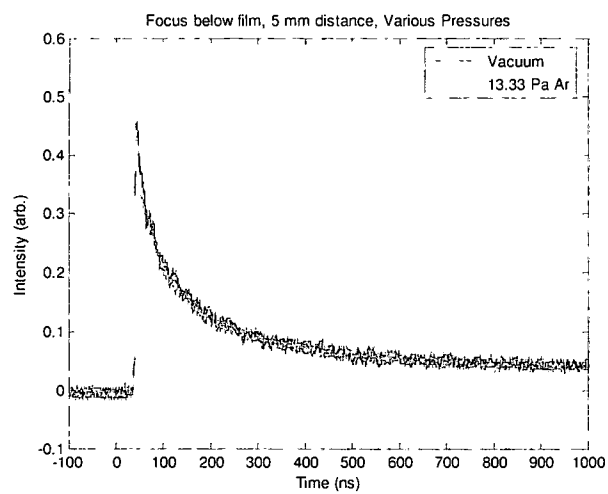


Figure 6.2. PMT signals from ablations with the laser focus below the film at various pressures.

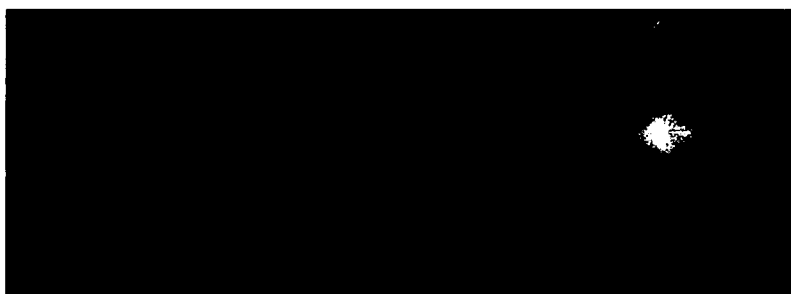


Figure 6.3. Gated camera image with a delay of 1 μ s, showing the distortion to the plume in higher pressures of background gas.

6.2 – Effect of Laser Focus Location

In examining the effect of changing the location of the focus of the laser, dramatically different results can be seen from the PMT data. With a background pressure of 13.33 Pa of argon, examining the data collected shortly after the laser pulse shows significantly different features. As can be seen in Figure 6.4, the signal from the ablation with the laser focus at the target contains three peaks, with speeds of 140.5 km/s, 57.3 km/s and 7.7 km/s. However, in lowering the laser focus to beneath the target, no such peaks can be seen in the same temporal range, as shown in Figure 6.5.

However, in when looking at longer temporal regions, distinctions can be seen in the data collected with the target away from focus. Shown in Figure 6.6, with a twenty-point moving average applied to the raw data to reduce the noise, a slight peak is evident, with a speed of 740.5 m/s. Looking at the same data collected for the laser focus at the film, Figure 6.7, no distinguishing characteristics are seen in longer time scales.

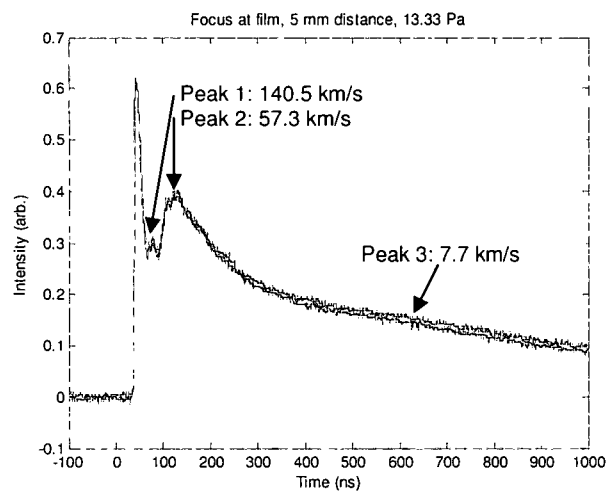


Figure 6.4. Peaks seen by PMT when the laser focus is at the target.

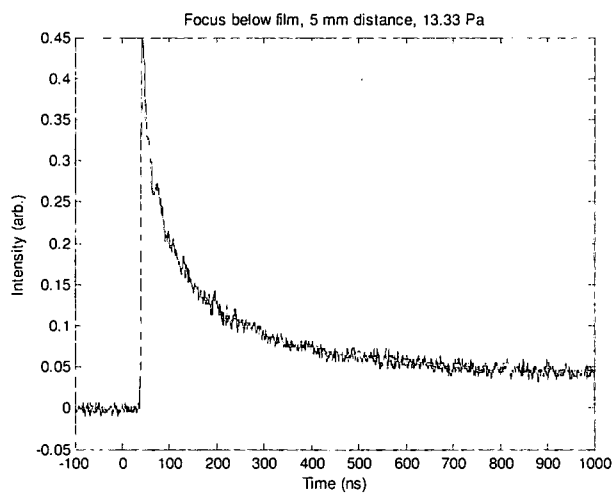


Figure 6.5. No peaks are seen in the same range when the laser focus is below the target.

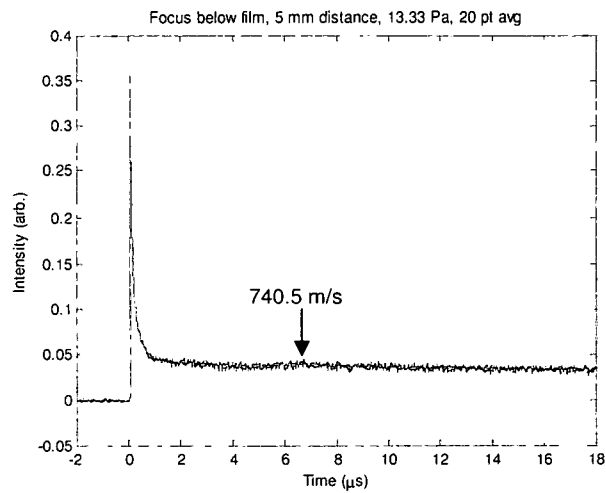


Figure 6.6. Slight peak seen in longer temporal regions when the laser focus is below target.

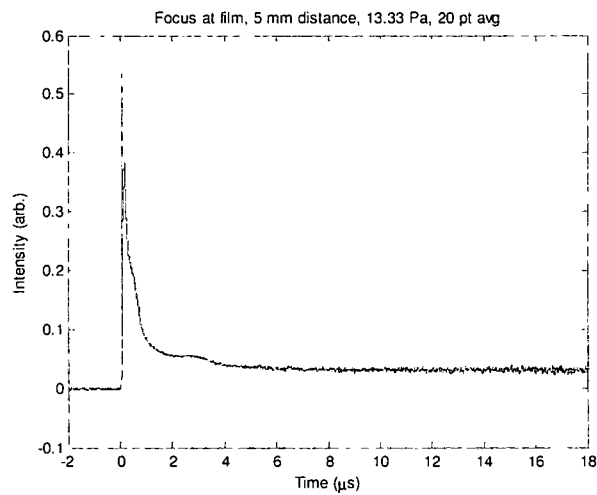


Figure 6.7. No peaks seen in the longer time scales when the laser focus is at the target.

6.2.1 – Laser Focus below the Target

This suggests that changing the location of the laser focus drastically changes the plume formation. With the laser focus below the film, the formation follows a more thermal process than when the focus is at the target. With the laser focus below the film, it appears as if the laser energy is absorbed by the target, the target melts and subsequently vaporizes into a gaseous plume, before traveling down towards the substrate. Due to interactions of the vapor with the background gas, the vaporized iron would condense and join together to form nanoparticles. The melting process would also cause the molten material to pool up into liquid puddles that would detach from the target surface and travel in a liquid state to strike the substrate. This can clearly be seen in the SEM micrographs of the particles, as evidence of splashing can be seen as well as small, round particles that likely were deposited onto the surface in a solid state.

This is supported by the PMT measurements. The initial heating, melting and evaporation are seen in the short time scale as a gradual reduction of the light intensity as the system cools and the material leaves the surface. There is only one peak at a relatively slow speed, which is indicative of larger particles, and similar to particle speeds from traditional PLA. In order to further analyze the speeds produced by the plume, the PMT intensity versus time signal was converted into a plot of intensity versus velocity. A Maxwell-Boltzmann distribution, described by the formula $f(v) = cv^2 e^{-mv^2/2kT}$ where c is a constant, m is the mass of one atom of iron, v is the velocity and k is Boltzmann's constant equal to 1.38×10^{-23} J/K, was fit to the velocity plot by varying the temperature parameter, T [53]. This gives a calculation of the temperature of the plume, and solving for its first derivative set equal to zero gives the maximum value, which is the most probable velocity of the atoms in the system [5].

The resultant plot of the velocity and the Maxwell-Boltzmann distribution can be seen in Figure 6.8. With a temperature of 950 K, the distribution closely approximates the area with the highest intensity seen with lower velocities; however, there is a tail, representative of high energy (fast velocity) particles that do not fit with the distribution. While this temperature is below the melting point of bulk iron (1811.2 K), the plume is not in an equilibrium state and will cool rapidly as it travels towards the substrate. Using this temperature, however, and calculating the most

probable velocity of the material from the equation $v = \left(\frac{2kT}{m} \right)^{1/2}$ gives a speed of 531.6 m/s, which corresponds to previous calculations of the plume velocity.

The gated camera images also show an active region right on the target at short time scales, that eventually forms a plume and detaches from the target to travel to the substrate on longer (μ s) timescales. Calculating the inherent camera delay from low pressure (1.33 Pa) images with short gate delays shows an 85.9 ns camera delay to be added to the gate delay in measuring the speed of the plume in the images. By plotting the intensity of the image and measuring the distance to the most intense region of the plume from the target at various gate delays confirm the speed calculations; showing that at a 1 μ s gate delay, the plume is traveling at a speed of 393.0 m/s as seen in Figure 6.9.

The measurements from the metal plate used to detect the charge of the plume also support this explanation. With the laser focus below the film, a charge was not detected, indicating that any material in the plume would predominantly be neutral. With the laser energy used in a heating and vaporizing capacity, the atomic structure of the film would not be changed to cause a charge in the material.

In examining the energy necessary to heat, melt and evaporate a 10 nm iron film, it is necessary to calculate the energy per pulse from the laser. With an average power of 0.151 mW, operating at a pulse repetition rate of 1.176 kHz, each pulse had energy of 128.4 μ J. Using a transmission spectrometer, the transmission of 1064 nm light through a 10 nm iron film was measured to be 55%. This indicates that 45% of the laser energy is absorbed by the target, or, put differently, 57.8 μ J per pulse are used in vaporizing the film.

In heating the film to vaporization, four different processes are present: heating the film from ambient temperature to iron's melting point ($\Delta T = 1513.2$ K, specific heat $c_p = 0.449$ J/gK), the phase change during melting (heat of fusion, $\Delta H_f = 13.81$ kJ/mol), heating the molten liquid to the boiling point ($\Delta T = 1323.0$ K, specific heat $c_p = 0.825$ J/gK) and finally vaporizing the film (heat of vaporization, $\Delta H_v = 416.30$ kJ/mol) [52, 54] as described in the sum

$$\Delta H = \int_{T_{amb}}^{T_m} c_p^s dT + \Delta H_f + \int_{T_m}^{T_b} c_p^l dT + \Delta H_v$$
 For the spot size of 200 by 240 μm , the volume of material removed is 377.0 μm^3 , and using iron's density of 7.87 g/cm^3 , a mass of 2.97×10^{-9} g of iron is present in each plume. Along with the molar mass of iron, 55.847 g/mol, it is found that the energy to vaporize one area is 28.1 μJ , half of the energy provided by the laser.

This is also supported by the SEM of the particles formed. As the ablation mechanism with the laser focus located below the target consists of melting and vaporizing the film, a number of the particles formed are irregular in shape and appear transparent, as they were deposited on the substrate in a molten form, creating splashes upon impact, as seen in Figure 6.10.

There is also no damage seen to the target support, shown in Figure 6.11. This shows that the energy absorbed from the laser pulse is utilized to melt and vaporize the film, without excess energy to cause damage to the support, which is in accordance with the calculation to determine the amount of energy necessary to vaporize the film.

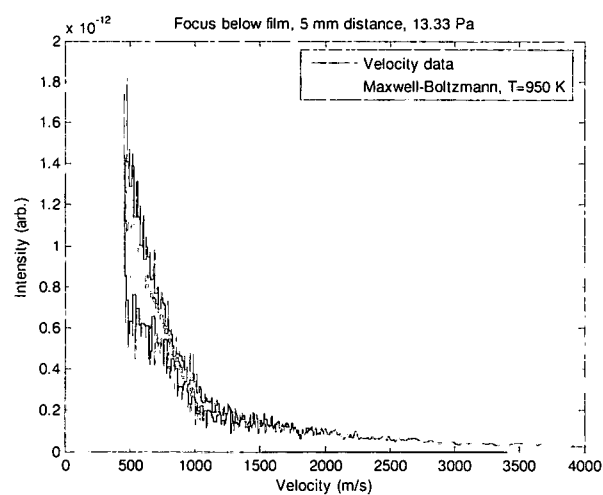


Figure 6.8. Velocity and Maxwell-Boltzmann distribution of PMT signal.

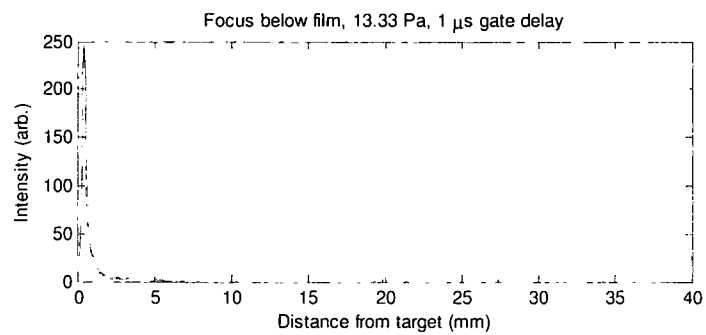
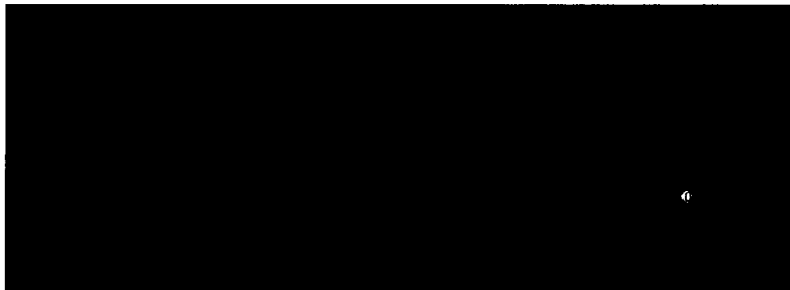


Figure 6.9. An intensity plot of the emission of the plume at a 1 μ s gate delay.



Figure 6.10. SEM micrograph of particles formed with the laser focal point below the target film. An example of an irregular, transparent particle is indicated with a white arrow. The scale bar is 2.00 μm .

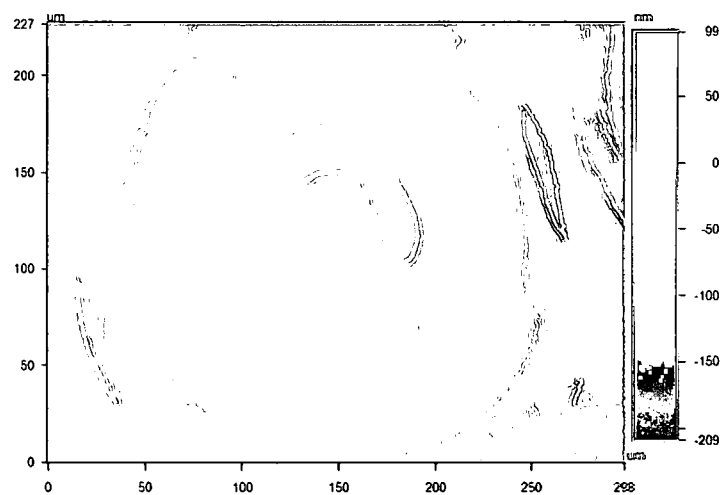


Figure 6.11. White light interferometer data showing the film removed from the substrate, in the reddish area, without residual damage.

6.2.2 – Laser Focus at the Target

In contrast, the ablations with the laser focal point at the target cannot be as easily explained. The optical images show that there are two constituents of the ablation, the first being significantly faster than the second, appearing to be completely resolved by 5 μ s. The second follows a temporal evolution nearly identical to that of the plume with the laser focus below the film.

In examining the first constituent, the PMT signal shows there are three distinct events passing in front of the slit after short delays from the laser pulse, and then no distinct peaks to indicate a large gathering of material for longer times. This suggests that the laser energy in the pulse is absorbed and has a high enough energy level to ionize the film. The first phase would be the laser pulse ionizing iron atoms in the film, seen as the first peak as the electrons excite the background pressure in the chamber. This would be the fastest event, and significantly less intense as detecting this event depends on the small probability that an electron would excite an argon atom. After the electrons leave the film, a large quantity of positively charged iron ions would remain, causing a Coulomb explosion of the like-charged, excited atoms repelling each other. This would be seen as the second peak in the PMT signal, slower than electrons due to the larger mass but still orders of magnitude faster than the previously seen nanoparticles, due to the repulsive forces. Without further investigation, the PMT data would suggest that the third peak seen would be small nanoparticles or groups of a few atoms, but looking at the charge collection plate measurements indicates a different explanation.

In examining the charge plate experimentation, three peaks are seen with speeds nearly identical to the PMT data, as shown in Figure 6.12. The first peak seen is the positive spike from when the laser struck the metal surface, ejecting electrons by the photoelectric effect and creating a net positive charge. Next, a negative charge is detected, as would be expected from electrons in a plasma plume. The positive iron atoms then create a strong positive net charge on the plate, and the material seen as the third PMT peak shows a negative charge. This indicates that the third peak may be composed of Rydberg atoms, metastable atoms with electrons in a very high energy level such that the electron is easily given up when it touches the metal surface via

Penning ionization [5]. These appear slower than the other iron ions as there are no repulsive forces to accelerate them apart.

Converting the signal detected by the PMT into a velocity plot that was subsequently fitted with a Maxwell-Boltzmann distribution, as described before and shown in Figure 6.13, gives a temperature for the plume of 8500 K, shown by the red curve. This is significantly hotter than the plume with the laser focus below the target, as well as significantly above the boiling point of bulk iron (3134.2 K). While the temperature is an approximation as this is not a system in equilibrium, this does indicate that a significant portion of the laser energy is being used to vaporize and heat the atoms. In looking at the most probable velocity of the plume, a speed of 1590.2 m/s is found, which is of the same order of magnitude of the ions found in the PMT and charge plate measurements. However, as there are two components within the plume, a second, shifted Maxwell-Boltzmann distribution [55] can be fit to a second curve seen in the velocity data, shown by the green curve. The formula for a shifted Maxwell-Boltzmann is given by $f(v) = cv^3 e^{-m(v-v_s)^2/2kT}$, where v_s is the streaming velocity. Here, the streaming velocity is 3600 m/s, and the second temperature is 40,000 K. This results in a most probable velocity of 3449.7 m/s. It should be noted that, even with both a Maxwell-Boltzmann and a shifted Maxwell-Boltzmann distribution, the velocity data is still not well described, as indicated by the tail representative of high energy particles.

While this explains the events shortly after the laser pulse, there still is an apparently uniform amount of light detectable by the PMT for many microseconds after the laser pulse. This would be the actual nanoparticles, formed on the edges of where the laser struck the target and creating the second constituent. As the beam possesses a Gaussian energy distribution, the edges of the laser would not possess the necessary energy to strip the atom of its electrons, causing the surrounding areas to vaporize and form nanoparticles while traveling to the substrate. As these particles would be neutral in charge, nothing would be detected by the metal plate measurements. The gated camera images also suggested that a dual process is likely, as two separate plumes are formed. The first, a plasma of electrons, ions and Rydberg atoms, would leave the surface quickly and disperse while the vaporizing and forming of nanoparticles would

still be occurring on the surface, following in a separate plume, seen as significantly slower than the first. The image taken in 13.33 Pa of argon 1 μ s after the laser trigger in Figure 6.14 clearly shows the dispersing first plasma with the second plume forming on the target surface behind it. As before, the speeds of each plume were measured by plotting the intensity profile of the camera images. As can be seen, the first plume has a speed of 7129.9 m/s while the second plume has a speed of 336.8 m/s, both within the same order of magnitude of the other speeds recorded by PMT. It is also interesting to note that the speed of the second plume, theorized to be nanoparticles formed by the edges of the laser pulse, is nearly identical to speeds seen when the laser focus is set below the film.

Examining the damage of the target evident in these conditions also shows evidence to support this understanding of the plume dynamics. In examining the ablated area of Figure 6.15, a damaged region is seen in the center, but no damage is evident around the perimeter of the area. It is important to note that the energy distribution of the beam shape is Gaussian in nature, and the center of the Gaussian, the region with the highest energy, is where the damage is evident. This is also the region where the first plume component would be formed, with the second component forming from the edges without evidence of damage. In this area, there would not have been a high enough energy density to damage the support, but still enough energy to vaporize the film.

As before, the energy necessary to heat the film to vaporization was calculated, with the only variation being the volume of material. As the spot size is smaller, measuring 100 by 150 μ m, the volume of material removed is 117.8 μ m³, or 0.93x10⁻⁹ g. This results in a necessary energy of 8.8 μ J to vaporize one ablation spot, while the laser provides approximately 6.5 times that energy, or 57.8 μ J. At least a portion of the excess energy will be absorbed by the vapor and seen as an increase in temperature, as described by the a fifth component of the sum,

$$\Delta H = \int_{T_{umb}}^{T_m} c_p^s dT + \Delta H_f + \int_{T_m}^{T_b} c_p^l dT + \Delta H_v + \int_{T_b}^{T_v} c_p^v dT .$$

Using the temperature fit by the Maxwell-

Boltzmann distribution, 8500K, which is still likely lower than the actual temperature immediately after the ablation due to plasma cooling and recombination, the change in temperature of the

vapor is 5365.8 K. With a specific heat for iron vapor (c_p) of 0.460 J/gK [52] the energy necessary to heat the vapor to the calculated temperature is 2.29 μ J, or a total energy of 11.07 μ J for heating the film from ambient temperature to a hot vapor. The discrepancy in the amount of energy used in the ablation as opposed to the energy absorbed by the film can be explained by inverse bremsstrahlung radiation. This is the phenomenon where incident photons from the laser are absorbed by the electrons in the plasma [5].

In examining the events of the ablation on an atomic level, it should be noted that the energy of each photon from the laser, operating at a wavelength of 1064 nm, has an energy of 1.17 eV, calculated from $E=h\nu$, where h is Planck's constant and ν is the frequency of the light. The first ionization energy of iron is 7.90 eV [52], which indicates that multiple photons are necessary to remove one electron from each atom. In this case, it is interesting to note that 7 photons are needed, which almost perfectly corresponds to the ratio of the energy of the absorbed laser pulse to the energy necessary to heat the material to vaporization.

However, due to the Gaussian energy distribution of the beam, it is not possible that every atom has only one electron removed. The atoms near the central region of the ablation area likely had multiple electrons removed, while the edges of the area likely did not ionize at all, and only melted and vaporized in a thermal process. This can be seen by examining the kinetic energy of the ions. For the ablation in 13.33 Pa of an argon background, a speed of 57.3 km/s was found for the peak of iron ions. Using $E = 0.5mv^2$ for the formula for kinetic energy, and the mass of the ablated material is 0.93×10^{-9} g, the resultant kinetic energy is 1.52 mJ. If it were to be assumed that each atom only loses one electron, the repulsive force between the ions would be given by $F = \frac{kq_1q_2}{r^2}$, where k is the Coulomb constant, $8.99 \times 10^9 \text{ Nm}^2/\text{C}^2$, and q_1 and q_2 are the charge of the ions; here each 1.60×10^{-19} C as one electron has been removed from each. The distance between them, r , is given by their lattice constant, 286.65 pm [52]. This gives a force of 2.8 nN. As $1 \text{ J} = 1 \text{ N} \cdot \text{m}$, multiplying the force by the distance between them, where the distance is an integer number multiple of the lattice spacing, will equal the kinetic energy of the ions. The integer number of spacing is equal to the number of ions in the plume, here 1.89×10^{15} ions. As a comparison, the number of atoms present in the ablation area of 100 by 150 μm by 10 nm thick is

5.02×10^{12} atoms. Although in these conditions the transparent support for the target also is damaged, adding material to the plume, it is illogical that the amount of material removed from the support could be equal to this difference. This shows that the calculations on the kinetic energy and force of repulsion in the Coulomb explosion predict there should be almost a thousand times more material present in the plume than can be present. This confirms that there is a smaller component in the plume with multiple ionization of the atoms with very strong repulsive forces to drive the ions apart at high speeds, while another portion of the plume is not highly ionized and would travel at slower speeds.

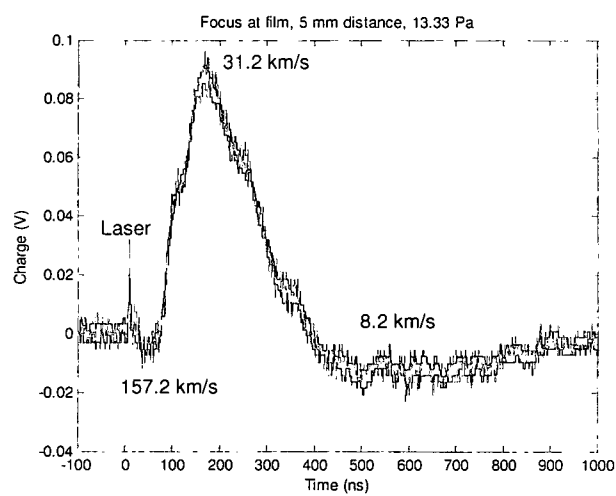


Figure 6.12. Plot of the charge of the metal plate with the laser focus at the film.

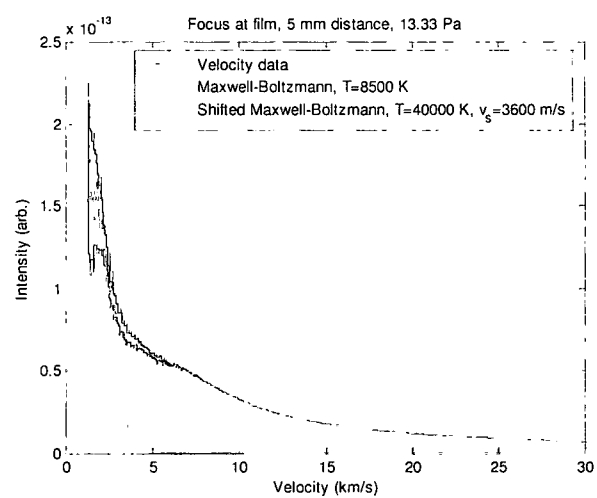


Figure 6.13. Velocity plot and Maxwell-Boltzmann distribution of the PMT signal.

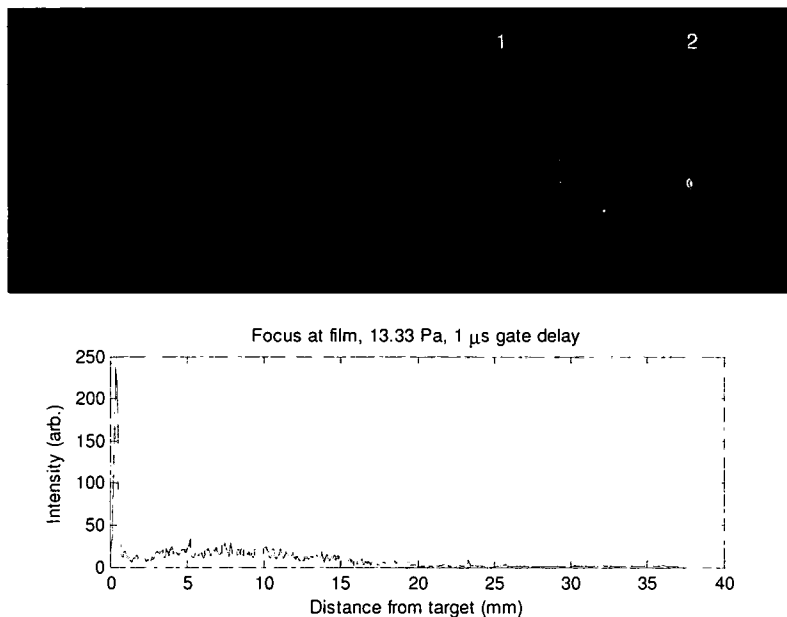


Figure 6.14. Image of the first plasma, indicated with the numeral 1, dispersing while the second plume forms on the target surface behind it, indicated with the numeral 2, with an intensity profile of the image.



Figure 6.15. White light interferometer data of an ablated spot with the laser focal point at the target.

CHAPTER 7

CONCLUSION

While Through Thin Film Ablation is still a new and relatively uncharacterized process, strides are being made to measure its properties and form a model of understanding. In examining the target and synthesized nanoparticles in two different setups, a significant difference was found when the focal point of the ablation laser was located at the target or approximately 5 mm below the target.

7.1 – Ablation with the Focal Point below the Target

With the focal point below the target, the particles appear small and separated, with some particles that show splashing from hitting the substrate while in a liquid state. In examining the plume formation, PMT and gated camera images showed a single plume of material traveling to the substrate at a relatively low speed of hundreds of meters per second. Charge measurements on this material show that the particles are neutral. This indicates that the laser energy is being absorbed by the target, causing the film to melt and vaporize before ejecting away from the target. As the vapors interact with each other and the background gases present in the chamber, the material recombines into particles less than 10 nm in diameter and deposit on the substrate. The mix of molten and solid particles seen is due to the change in initial temperature across the target, where the molten particles would form from the recombination and cooling vapor, and the solid particles would be from the edges of the ablation area with a lower temperature.

7.2 – Ablation with the Focal Point at the Target

Placing the focal point of the laser at the target creates small, separated particles that appear spherical when deposited on the substrate. The target itself shows damage in the center of the ablated area, with material removed from the transparent support. The plume formation is also decidedly different from having the laser focus at the target. The gated camera images show

two separate, distinct plume constituents, the first traveling at a high speed of tens of kilometers a second, and a second traveling at hundreds of meters a second. The PMT measurements show that the first constituent contains three different events, which was confirmed by measuring the change in net charge of each event. It was found that the laser energy is absorbed by the film, and the electrons are removed from the film first, leaving positively charged iron atoms, which repel each other to form a Coulomb explosion, the second event. The third event is Rydberg atoms, which appear slower than the iron ions and give a slight negative charge.

The second constituent is from the edges of the ablation area, where the energy is not as intense, allowing the material to follow the same melting and vaporization process seen for the conditions with the laser focal point below the target. While recombination of the ions from the first constituent would create some nanoparticles, the majority of the particles are formed within the second constituent. This melting and vaporization would contain the neutrally charged nanoparticles, which cool during their travel to the substrate, depositing in what appears to be mostly solid form.

Understanding the dynamics of the plume formation and its effect on the resultant particles provides valuable clues to understanding the TTFA process. A thorough understanding of this process allows for the discovery of a mechanism to provide control over the resultant particles, their properties, placement and thus potential uses.

CHAPTER 8

RECOMMENDATIONS FOR FUTURE WORK

In order to better understand the TTFA process, further work would be required. In refining the theory of the plume formation, the ionic and excited species created in the process should be identified with a spectrometer. A gated spectrometer would be able to identify the excited argon present when material collides with the background gas, as well as excited iron created in the ablation process. The multiple ionization should be verified with a mass spectrometer to determine the level of ionization present in the plume. This would likely further corroborate the theories presented here, and provide a means to identify contaminants in the system in situ.

A detailed understanding of the plume formation would also be useful in predicting the most probable size of the particles. It has been shown that some particle properties, such as shape, can be controlled by plume dynamics, while others, such as agglomeration, can be controlled by using a background gas. If a detailed understanding of these properties were achieved, it would be possible to predict the particle size and distribution on the substrate, which would provide a great control for specific applications.

A potential application would be to add a carbon source to the ablation. As the plume has been shown to be hot, it should have sufficient energy to split the carbon into an atomic form, and grow a carbon nanotube in the plume, nucleating from a particle. Another potential application would be to control the particle size within tight tolerances and deposit the material using a direct writing process. Due to the relative directionality of the plume, particles of a specific size could be deposited when the material is needed, and not placed in other areas.

REFERENCES

- [1] D. Gubencu, Opt. Laser Tech. 37, 577 (2005)
- [2] D. Breitling, A. Ruf, F. Dausinger, Proc. of SPIE, 5339
- [3] U. Klug, B. Kamlag-Rhan, J. Koch, R. Knappe, U. Stute, B. Chichkov, ICALEO Cong. Proc. (2006)
- [4] C. Momma, S. Nolte, B.N. Chichkov, F. v. Alvensleben, A. Tünnermann. Appl. Surf. Sci. 109-110, 15 (1997)
- [5] Sree Harsha, KS. Principles of physical vapor deposition of thin films. 1st ed. London: Elsevier; 2006.
- [6] Waser, Rainer, ed. Nanoelectronics and Information Technology. 2nd ed. Weinheim: Wiley-VCH; 2005.
- [7] D. H. Lowndes, D. B. Geohegan, A. A. Puretzky, D.P. Norton, C.M. Rouleau, Science. 273, 898 (1996)
- [8] Mahan, John E. Physical vapor deposition of thin films. New York: Wiley; 2000.
- [9] J. C. Alonso, R. Diamant, P. Castillo, M.C. Acosta-Garcia, N. Batina, E. Haro-Poniatowski, Appl. Surf. Sci. 255, 4933 (2009)
- [10] A. A. Puretzky, H. Schittenhelm, X. Fan, M. J. Lance, L. F. Allard, D. B. Geohegan, Phys. Rev. B. 65, 245425 (2002)
- [11] C.D. Scott, S.Arepalli, P. Nikolaev, R. E. Smalley, Appl. Phys. A. 72, 573 (2001)
- [12] R. H. Baughman, A. A. Zakhidov, W. A. de Heer, Science. 297, 787 (2002)
- [13] X. Z. Liao, A. Serquis, Q. X. Jia, D. E. Peterson, Y. T. Zhu, Appl. Phys. Lett. 82, 2694 (2003)
- [14] A. G. Nasibulin, P. V. Pikhista, H. Jiang, E. I. Kauppinen, Carbon. 43, 2251 (2005)
- [15] A. Moisala, A. G. Nasibulin, E. I. Kauppinen, J. Phys. Condens. Matter. 15, S3011 (2003)

- [16] M. Yudasaka, T. Ichihashi, T. Komatsu, S. Iijima, Chem. Phys. Lett. 299, 91 (1999)
- [17] P. T. Murray, E. Shin, Mater. Lett. 62, 4336 (2008)
- [18] M.N. Ashfold, F. Claeysens, G.M. Fuge, S.J. Henley, Chem. Soc. Rev. 33, 23 (2004)
- [19] R. K. Singh, J. Narayan, Phys. Rev. B. 41, 8843 (1990)
- [20] A. B. Brailovsky, S. V. Gaponov, V. I. Luchin, Appl. Phys. A. 61, 81 (1995)
- [21] S. Witanachchi, P. Mukherjee, J. Vac. Sci. Technol. A. 13 1171 (1995)
- [22] J. A. Greer, M. D. Tabat, J. Vac. Sci. Technol. A. 13, 1175 (1995)
- [23] A. Semerok, B. Salle, J.F. Wagner, G. Pette, Laser and Particle Beams. 20, 67 (2002)
- [24] B. Salle, C. Chaleard, V. Detalle, J.L. Lacour, P. Mauchien, C. Nouvellon, A. Semerok, Appl. Surf. Sci. 138-139, 302 (1999)
- [25] G. Koren, A. Gupta, R. J. Baseman, M. I. Lutwyche, R. B. Laibowitz, Appl. Phys. Lett. 55, 2450 (1989)
- [26] J. Gudde, J. Hohlfeld, J. G. Muller, E. Matthias, Appl. Surf. Sci. 127-129, 40 (1998)
- [27] D. W. Fradin, N. Bloemergen, J. P. Letellier, Appl. Phys. Lett. 22, 635 (1973)
- [28] V. Temnov, K. Sokolowski-Tinten, P. Zhou, D. von der Linde, J. Opt. Soc. 23, 1954 (2006)
- [29] Y. Lai, N. Cheung, Rev. Sci. Instrum. 64, 1606 (1993)
- [30] X. L. Zhou, W. Wen, J. S. Zhang, D. B. Sun, Surf. Coat, Tech. 190, 260 (2005)
- [31] S. K. Lee, K. K. Yoon, K. H. Whang, S. J. Na, Surf. Coat, Tech. 113, 63 (1999)
- [32] A. Neogi, R.K. Thareja, Phys. Plasmas 6, 365 (1999)
- [33] O. Barnes, P. T. Murray, T. Haugan, R. Rogow, G. Perram, Physica. 377, 578 (2002)
- [34] A. G. Guidoni, R. Kelly, A. Mele, A. Miotello, Plasma Sources Sci. Technol. 6, 260 (1997)
- [35] S. S. Harilal, M. S. Tillack, B. O' Shay, C. V. Bindhu, F. Najmabadi, Phys. Review E. 69, 016413 (2004)
- [36] G. Han, P. T. Murray, J. Appl Phys. 88, 1184 (2000)
- [37] R. P. van Ingen, J. Appl. Phys. 79 467 (1996)
- [38] M. Joseph, N. Sivakumar, D. D. A. Raj, C. K. Mathews, J. Nucl. Mater. 247, 21 (1997)
- [39] K. Sokolowski-Tinten, J. Bialkowski, A. Cavalleri, D. von der Linde, A. Oparin, J. Meyer-ter-Vehn, S. I. Anisimov, Phys. Review Lett. 81, 224 (1998)

- [40] R. Teghil, A. Santagata, A. De Bonis, G. Albano, P. Villani, D. Spera, G. Parisi, A. Galasso, Phys. Scripta 78, 058113 (2008)
- [41] O. Albert, S. Roger, Y. Glinec, J.C. Loulergue, J. Etchepare, C. Boulmer-Leborgne, J. Perrière, E. Millon, Appl. Phys. A. 76. 319 (2003)
- [42] S. Amoruso, R. Bruzzese, M. Vitiello, N. N. Nedialkov, P. A. Atanasov, J. Appl. Physc. 98, 044907 (2005)
- [43] T. E. Itina, J. Hermann, P. Delaporte, M. Sentis, Thin Solid Films. 453-454, 513 (2004)
- [44] C. Momma, B. Chichkov, S. Nolte, F. von Alvensleben, A. Tunnermann, H. Welling, B. Wellegehausen, Optics Communications. 129, 134 (1996)
- [45] A. Semerok, C. Chaleard, V. Detalle, J. L. Lacour, *et al.* Appl. Surf. Sci. 138-139, 311 (1999)
- [46] S. Nolte, C. Momma, H. Jacobs, A. Tunnermann, B. N. Chichkov, B. Wellegehaussen, H. Welling, J. Opt. Soc. Am B. 14, 2716 (1997)
- [47] D. von der Linde, K. Sokolowski-Tinten, J. Bialkowski, Appl. Surf. Sci. 109-110, 1 (1997)
- [48] D. von der Linde, H. Schuler, J. Opt. Soc. Am. B. 13, 216 (1996)
- [49] K. Bailey, Unpublished Results
- [50] P.T. Murray, E. Shin, Private Communications
- [51] W.S. Rasband. ImageJ [computer program]. U. S. National Institutes of Health, Bethesda, Maryland, USA: 1997-2009.
- [52] Chemical Rubber Company. CRC handbook of chemistry and physics. 1978.
- [53] P. A. Tipler. Physics for scientists and engineers. 4th ed. New York: W.H. Freeman and Co., 1999.
- [54] M. Beutl, G. Pottlacher, H. Jäger, Int. J. Thermophys. 15, 1323 (1994)
- [55] J. P. Zheng, Z. Q. Huang, D. T. Shaw, H. S. Kwok, Appl. Phys. Lett. 54, 280 (1989)